

1 Coastal Atmosphere & Sea Time Series (CoASTS) and Bio-Optical mapping of
2 Marine optical Properties (BiOMaP): the CoASTS-BiOMaP dataset.

3

4

Giuseppe Zibordi¹ and Jean-François Berthon²

5

6

¹*National Aeronautics and Space Administration, Goddard Space Flight Center, MD USA*

7

²*Joint Research Centre of the European Commission, Ispra, Italy*

8

9

Correspondence to: Giuseppe Zibordi (giuseppe.zibordi@eoscience.eu)

10
11
12
13
14
15
16
17
18
19
20
21
22
23
24
25

ABSTRACT

The *Coastal Atmosphere & Sea Time Series* (CoASTS) and the *Bio-Optical mapping of Marine optical Properties* (BiOMaP) programs produced bio-optical data supporting satellite ocean color applications for more than two decades. Specifically, relying on the Acqua Alta Oceanographic Tower (AAOT) in the northern Adriatic Sea, from 1995 till 2016 CoASTS delivered time series of marine water apparent and inherent optical properties, in addition to the concentration of major optically significant water constituents. Almost concurrently, from 2000 till 2022 BiOMaP produced equivalent spatially distributed measurements across major European Seas. Both, CoASTS and BiOMaP applied standardized instruments, measurement methods, quality control schemes and processing codes to ensure temporal and spatial consistency to data products. This work presents the CoASTS and BiOMaP near surface data products, named CoASTS-BiOMaP, of relevance for ocean color bio-optical modelling and validation activities.

26 1. Introduction

27 The validation of primary (*i.e.*, radiometric) and derived (*e.g.*, phytoplankton pigments
28 concentration) satellite data products, as well as the development of bio-optical algorithms
29 linking radiometric data to the inherent optical properties or to the concentration of natural water
30 optically significant constituents, require accurate and comprehensive *in situ* bio-optical
31 measurements (*e.g.*, see Werdell and Bailey 2007). Anticipating this need for the Sea-Wide
32 Field-of-View (SeaWiFS) ocean color mission, during the 90s several measurement programs
33 were established to gather bio-optical data representative of the world marine waters. Among
34 these, the *Coastal Atmosphere & Sea Time Series* (CoASTS) and the *Bio-Optical mapping of*
35 *Marine optical Properties* (BiOMaP) measurement programs implemented by the Marine
36 Optical Laboratory (Belward et al. 2022) of the Joint Research Center (JRC) in collaboration
37 with a number of European institutions, produced comprehensive *in situ* bio-optical
38 measurements of relevance for satellite ocean color applications. While CoASTS benefited of the
39 Acqua Alta Oceanographic Tower (AAOT) in the northern Adriatic Sea to generate time-series
40 data at a fixed coastal site (Berthon et al. 2002; Zibordi et al. 2002), BiOMaP relied on
41 oceanographic ships to collect spatially distributed measurements across various European Seas
42 (Berthon et al. 2008, Zibordi et al. 2011). Both CoASTS and BiOMaP endorsed standardization
43 of instruments, measurement methods, quality control schemes and processing codes to enforce
44 consistency to temporally and spatially distributed data products. It is still recognized that some
45 of the measurement methods primarily implemented for optically complex coastal waters, may
46 not warrant the desirable high accuracy in oligotrophic clear waters.

47 Overall, CoASTS and BiOMaP data extend over a period exceeding two decades and
48 constitute a unique dataset for bio-optical investigations across a variety of water types with
49 potential application to climate change studies. Objective of this work is to introduce the
50 CoASTS and BiOMaP derived data products relevant for satellite ocean color applications.
51 Specifically, the near-surface data products with spectral values restricted to key ocean colour
52 center-wavelengths are presented together with a description of the measurement and data
53 reduction methods.

54 55 2. The CoASTS and BiOMaP programs

56 CoASTS and BiOMaP were conceived as complementary programs: CoASTS focused on
57 the generation of time-series of reference data from a fixed coastal site showing significant
58 seasonal cycles and moderate bio-optical complexity (Berthon et al. 2002); conversely BiOMaP
59 covered a variety of marine regions exhibiting very diverse bio-optical regimes, but with limited
60 temporal representativity (Berthon et al. 2008).

61 The use of an oceanographic tower as logistic platform for comprehensive optical and
62 bio-geochemical measurements, when compared to oceanographic ships, does not allow for
63 spatially extended observations. However, it offers the unique opportunity of a very stable
64 measurement platform enabling easy control of the deployment geometry of optical instruments
65 with respect to the structure. Specifically, regardless of sea state, the use of the AAOT as
66 measurement platform made possible deploying optical sensors relying on tower–sensor–Sun
67 geometry favouring the application of corrections for the minimization of potential
68 superstructure perturbations in radiometric data (Zibordi et al. 1999, Doyle and Zibordi 2002).

69 CoASTS measurements are representative of marine frontal regions exhibiting
70 occurrence of waters with optical properties largely determined by phytoplankton and its
71 degradation components (*i.e.*, Case 1 waters), as wells as optically complex waters characterized

72 by moderate concentrations of sediments and coloured organic matter (CDOM), with bio-optical
73 variability determined by the impact of local currents, seasonal changes in biological regimes
74 and rivers discharge (Berthon et al. 2002).

75 CoASTS measurements took place with monthly occurrence since 1995. However, from
76 2001 and up to the end of the measurement program in 2016, the frequency of field
77 measurements was reduced to one every 2-3 months. Each comprehensive data collection —
78 called a *station* — included in-water optical and hydrographic profiles, seawater samples at
79 different depths (*i.e.*, near surface, 8 m and 14 m), meteorological data, and visual observations
80 of cloud cover and sea state. CoASTS comprises 176 field campaigns leading to 883
81 measurement stations. Still, only CoASTS campaigns and stations performed from December
82 1998 onward (*i.e.*, 125 and 617, respectively) fulfil the requirement of measurements
83 standardization.

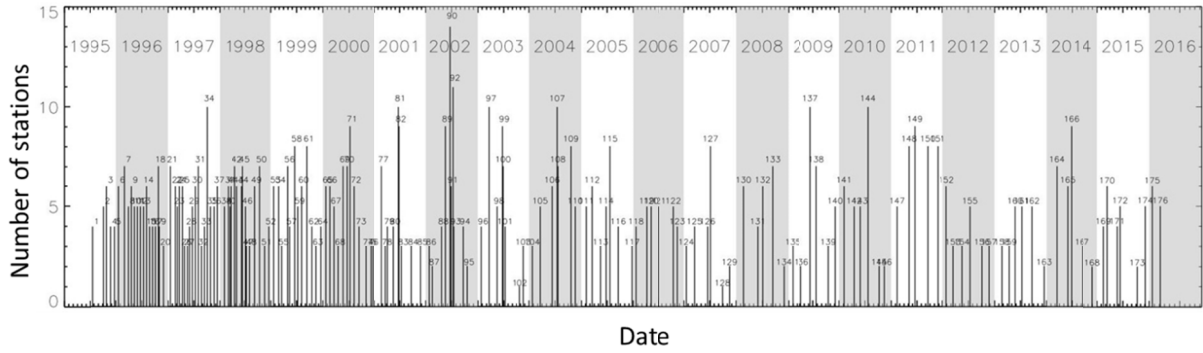
84 Spatially distributed measurements are best possible using oceanographic ships. Because
85 of this, BiOMaP measurements were performed relying on research vessels across a variety of
86 bio-optical regions (see Berthon et al. 2008): the Baltic Sea exhibiting waters dominated by a
87 high concentration of CDOM; the Adriatic Sea, Black Sea, North Sea (including the English
88 Channel), Ligurian Sea, Iberian Shelf and the Greenland Sea, characterized by a variety of
89 optically complex waters determined by diverse concentrations of CDOM and suspended
90 particulate matter (*SPM*); the Eastern and Western Mediterranean oligotrophic and mesotrophic
91 Seas with optical properties largely determined by phytoplankton and its degradation
92 components.

93 BiOMaP, encompassing 36 bio-optical oceanographic campaigns and 1915 measurement
94 stations, started in 2000 and ended in 2022. It is mentioned that some measurements from 33
95 BiOMaP stations performed in the Black Sea during 2011 were included in an independent
96 dataset constructed to support the validation of satellite data products (Valente et al. 2016).

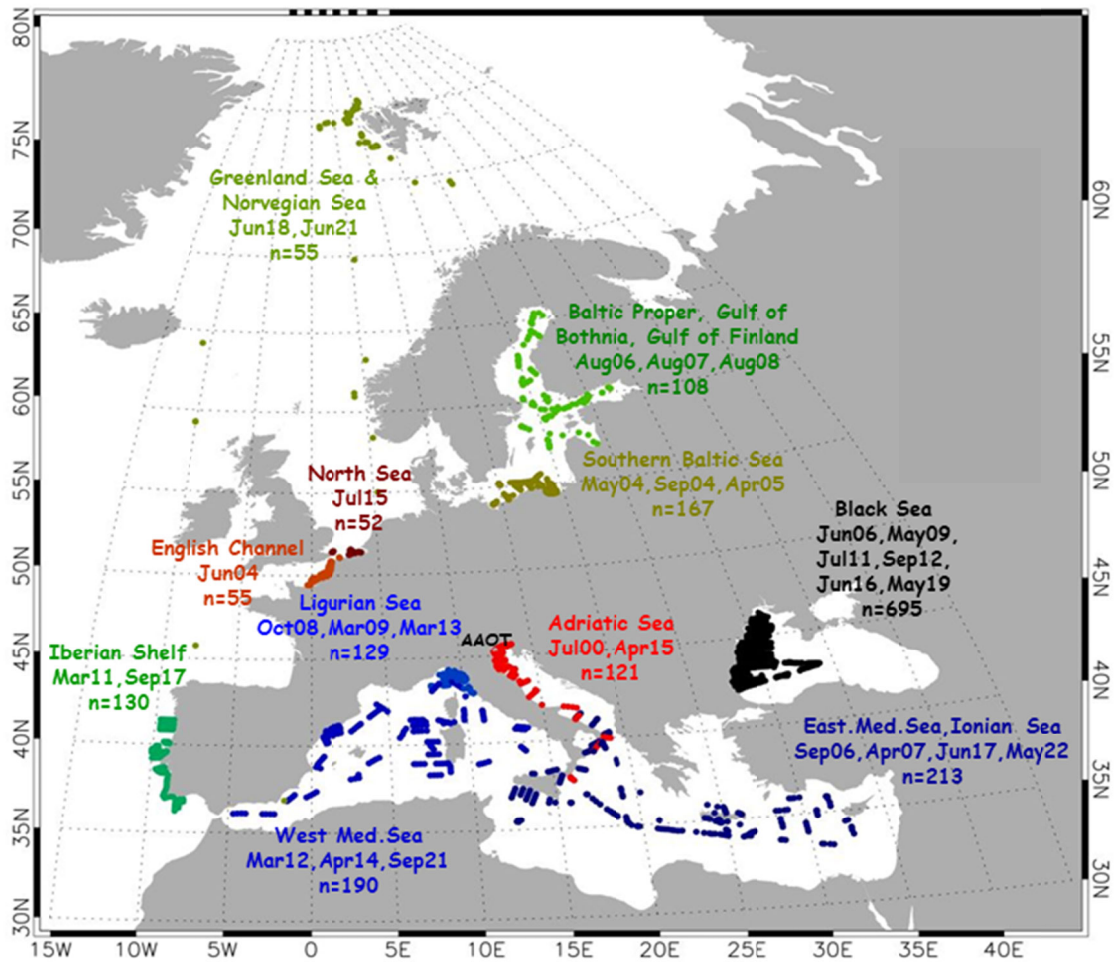
97 As already anticipated, measurement consistency between the CoASTS and BiOMaP
98 programs was achieved using identical field and laboratory instrumentation, and applying the
99 same consolidated methods, quality control schemes and processing codes. Consequently,
100 BiOMaP measurements performed during each station exhibit equivalence with those of
101 CoASTS, except for restricting the collection of water samples to the near surface. Finally,
102 superstructure perturbations in BiOMaP radiometric data were avoided by operating optical
103 radiometers on free-fall profilers deployed at some distance from ships (IOCCG 2019).

104 Figure 1 shows the temporal evolution of CoASTS measurement campaigns and the number
105 of stations per campaign. These latter were largely benefitting of sea state conditions allowing
106 access to the tower. Figure 2 shows the overall distribution of BiOMaP stations across the
107 various European Seas.

108
109



110
 111 Figure 1. CoASTS measurement campaigns (176 total, 125 since December 1998) and stations
 112 (883 total, 637 since December 1998) completed between 1995 and 2016.
 113



114
 115 Figure 2. BiOMaP oceanographic campaigns (36) and measurement stations (1915) performed
 116 between 2000 and 2022.

117 Table 1. The CoASTS measurement program: campaign identifiers, marine region, years,
 118 number of stations, research platform, collaborating institution.
 119

| Campaign ID | Location | Year | Stations # | Research platform | Collaborating Institution |
|-------------|------------------------------|-----------|------------|-----------------------------------------|----------------------------------------|
| V03-V99 | Northern Adriatic Sea (AAOT) | 1998-2011 | 481 | <i>Acqua Alta Oceanog. Tower (AAOT)</i> | Italian National Research Council (IT) |
| W01-W28 | Northern Adriatic Sea (AAOT) | 2011-2016 | 136 | <i>Acqua Alta Oceanog. Tower (AAOT)</i> | Italian National Research Council (IT) |

120
 121
 122
 123
 124
 125

Table 2. The BiOMaP measurement program: campaign identifiers, marine regions, year, number of stations, research vessels, collaborating institutions.

| Campaign ID | Region | Year | Stations # | Research vessel | Collaborating Institution |
|-------------|-------------------------|------|------------|----------------------------------------|---------------------------------------------------------|
| A01 | Adriatic Sea (ADRS) | 2000 | 55 | <i>R/V Friuli-Venezia Giulia (FVG)</i> | University of Trieste (IT) |
| A02 | Adriatic Sea (ADRS) | 2014 | 66 | <i>R/V Minerva-1</i> | Italian National Research Council (IT) |
| B01 | Baltic Sea (BLTS) | 2004 | 52 | <i>R/V Oceania</i> | Institute of Oceanology (PL) |
| B02 | Baltic Sea (BLTS) | 2004 | 52 | <i>R/V Oceania</i> | Institute of Oceanology (PL) |
| B03 | Baltic Sea (BLTS) | 2005 | 63 | <i>R/V Oceania</i> | Institute of Oceanology (PL) |
| B04 | Baltic Sea (BLTS) | 2006 | 23 | <i>R/V Aranda</i> | Institute of Marine Research (FI) |
| B05 | Baltic Sea (BLTS) | 2007 | 38 | <i>R/V Aranda</i> | Institute of Marine Research (FI) |
| B06 | Baltic Sea (BLTS) | 2008 | 47 | <i>R/V Aranda</i> | Institute of Marine Research (FI) |
| E01 | Eastern Med. Sea (EMED) | 2006 | 62 | <i>R/V Urania</i> | Italian National Research Council (IT) |
| E02 | Eastern Med. Sea (EMED) | 2007 | 69 | <i>R/V Urania</i> | Italian National Research Council (IT) |
| E03 | Eastern Med. Sea (EMED) | 2017 | 51 | <i>R/V Minerva-1</i> | Italian National Research Council (IT) |
| E04 | Eastern Med. Sea (EMED) | 2022 | 31 | <i>R/V Philia</i> | Hellenic Centre for Marine Research (GR) |
| I01 | Iberian Shelf (IBSH) | 2011 | 68 | <i>NRP Almirante Gago Coutinho</i> | Portuguese Hydrographic Institute (PT) |
| I02 | Iberian Shelf (IBSH) | 2017 | 62 | <i>NRP Almirante Gago Coutinho</i> | Portuguese Hydrographic Institute (PT) |
| K01 | Black Sea (BLKS) | 2006 | 93 | <i>R/V Akademik</i> | Institute of Oceanology (BG) |
| K02 | Black Sea (BLKS) | 2009 | 73 | <i>R/V Akademik</i> | Institute of Oceanology (BG) |
| K03 | Black Sea (BLKS) | 2009 | 40 | <i>R/V Akademik</i> | Institute of Oceanology (BG) |
| K04 | Black Sea (BLKS) | 2011 | 38 | <i>R/V Mare Nigrum</i> | National Institute of Marine Geology and Geocology (RO) |
| K05 | Black Sea (BLKS) | 2011 | 24 | <i>R/V Akademik</i> | Institute of Oceanology (BG) |

| | | | | | |
|-----|------------------------------------|------|----|-------------------------------|--------------------------------------------------|
| K06 | Black Sea (BLKS) | 2011 | 59 | <i>R/V Akademik</i> | Institute of Oceanology (BG) |
| K07 | Black Sea (BLKS) | 2012 | 93 | <i>R/V Akademik</i> | Institute of Oceanology (BG) |
| K08 | Black Sea (BLKS) | 2012 | 14 | <i>R/V Akademik</i> | Institute of Oceanology (BG) |
| K09 | Black Sea (BLKS) | 2016 | 54 | <i>R/V Akademik</i> | Institute of Oceanology (BG) |
| K10 | Black Sea (BLKS) | 2016 | 83 | <i>R/V Akademik</i> | Institute of Oceanology (BG) |
| K11 | Black Sea (BLKS) | 2019 | 80 | <i>R/V Akademik</i> | Institute of Oceanology (BG) |
| K12 | Black Sea (BLKS) | 2019 | 44 | <i>R/V Akademik</i> | Institute of Oceanology (BG) |
| L01 | Ligurian Sea (LIGS) | 2008 | 41 | <i>R/V Alliance</i> | Undersea Research Center (NATO) |
| L02 | Ligurian Sea (LIGS) | 2009 | 63 | <i>R/V Alliance</i> | Undersea Research Center (NATO) |
| L04 | Ligurian Sea (LIGS) | 2013 | 25 | <i>R/V Alliance</i> | Undersea Research Center (NATO) |
| N01 | English Channel & North Sea (NORS) | 2004 | 55 | <i>R/V Côtes de la Manche</i> | Université du Littoral Côte d'Opale (FR) |
| N02 | North Sea (NORS) | 2015 | 52 | <i>R/V Belgica</i> | Royal Belgian Institute of Natural Sciences (BE) |
| O01 | Western Med. Sea (WMED) | 2012 | 73 | <i>R/V Urania</i> | Italian National Research Council (IT) |
| O02 | Western Med. Sea (WMED) | 2014 | 64 | <i>R/V Urania</i> | Italian National Research Council (IT) |
| O03 | Western Med. Sea (WMED) | 2021 | 53 | <i>R/V Garcia del Cid</i> | Institute of Marine Science (ES) |
| P01 | Greenland Sea (GRLS) | 2018 | 15 | <i>R/V Alliance</i> | Undersea Research Center (NATO) |
| P03 | Greenland Sea ¹ (GRLS) | 2021 | 40 | <i>R/V Alliance</i> | Italian Hydrographic Institute (IT) |

¹ It includes stations from the Norwegian Sea.

126
127
128
129
130
131
132
133
134
135
136
137
138
139
140
141
142

3. Measurements overview

CoASTS and BiOMaP core data comprise *in situ* and laboratory measurements performed on samples prepared in the field. The firsts include:

- a. Multispectral profiles of upwelling nadir radiance $L_u(z,\lambda)$, downward irradiance $E_d(z,\lambda)$, and upward irradiance $E_u(z,\lambda)$, where z indicates the depth and λ the center-wavelength of each spectral band;
- b. Multispectral above-water downward irradiance $E_s(t,\lambda)$ acquired during in-water profiling (where t is the time corresponding to the depth z) and diffuse sky irradiance $E_i(t,\lambda)$ acquired at the end of each station with an irradiance sensor operated in conjunction with a rotating shadow band;
- c. Multispectral profiles of beam attenuation $c(z,\lambda)$, absorption $a(z,\lambda)$ and backscattering $b_b(z,\lambda)$ coefficients, commonly restricted to the first 25 m depth for BiOMaP and 15 m for CoASTS;
- d. Profiles of water temperature $T_w(z)$ and salinity $S_w(z)$, also restricted to the first 25 m depth for BiOMaP and 15 m for CoASTS;

- 143 e. Meteorological data including wind speed W_s in addition to cloud cover C_c and sea state
144 S_s observations.
145 The laboratory measurements performed on field samples, complementary to the *in situ* ones,
146 are:
147 f. Spectral *in vivo* particulate absorption coefficients $a_{ph}(\lambda)$ for the pigmented and $a_{dt}(\lambda)$ for
148 the non-pigmented particles;
149 g. Spectral CDOM absorption coefficient $a_{ys}(\lambda)$;
150 h. Phytoplankton pigments concentration;
151 i. Suspended particulate matter concentration *SPM*.

153 4. Measurements and data reduction methods

154 Information on measurement methods and data reduction are summarized in the following
155 subsections.

156 4.1 Radiometric products

157 CoASTS in-water radiometric measurements of $L_u(z,\lambda)$, $E_d(z,\lambda)$, $E_u(z,\lambda)$ were performed
158 with the Wire-Stabilized Profiling Environmental Radiometer (WiSPER) using Satlantic
159 (Halifax, Canada) OCR/OCI-200 multispectral radiometer series. Concurrently, above-water
160 $E_s(t,\lambda)$ and $E_i(t,\lambda)$ measurements were also collected with OCI-200 radiometers. In the case of
161 BiOMaP, the equivalent measurements were performed using miniPRO and microPRO Satlantic
162 custom designed free-fall profilers equipped with OCR/OCI-200 or alternatively OCR-507
163 multispectral radiometers. All radiometric quantities were measured with 6 Hz acquisition rate at
164 spectral bands relevant for ocean color applications with 10 nm bandwidth and nominal center-
165 wavelengths at 412, 443, 490, 510, 555, 665 and 683 nm. WiSPER data were gathered with a
166 deployment speed of 0.1 m s^{-1} . Conversely, the deployment speed of the free-fall systems
167 generally varied in the range of approximately $0.3\text{-}0.4 \text{ m s}^{-1}$. The collection of in-water
168 radiometric measurements with low tilt and as close as possible to the surface, was always
169 attempted to ensure best retrieval of subsurface radiometric values through the extrapolation of
170 profile data.
171

172 The regular absolute radiometric calibration of field optical radiometers was performed at
173 the JRC Marine Optical Laboratory using 1000W FEL lamps traceable to the National Institute
174 of Standards and Technology (NIST) or alternatively the National Physical Laboratory (NPL).
175 While CoASTS radiometers were re-calibrated on a six-monthly basis, BiOMaP radiometers
176 were calibrated before and after each oceanographic campaign. Regular inter-calibrations
177 between the JRC Marine Optical Laboratory and the National Aeronautics and Space
178 Administration (NASA) performed within the framework of the Ocean Color component of the
179 Aerosol Robotic Network (AERONET-OC), ensured continuous verification of the accuracy of
180 the calibration process (Zibordi et al. 2021).

181 Data pre-processing included: *i.* the application of absolute calibration coefficients and
182 immersion factors for in-water radiometers (Zibordi et al. 2004; Zibordi 2006); *ii.* the removal of
183 in-water and in-air data exhibiting tilt higher than 5° (this was confidently established from 2009
184 for BiOMaP $E_s(t,\lambda)$ and $E_i(t,\lambda)$); *iii.* limited to BiOMaP, the composition of successive profile
185 data typically collected within a 5 min interval to create multi-cast combined profiles to increase
186 the number of measurements per unit depth and consequently improve the precision of
187 extrapolated values; and *iv.* the correction of in-air irradiance data for the non-cosine response of
188 collectors (see Zibordi and Bulgarelli 2007). Additional corrections for sensors non-ideal

189 performance, such as out-of-band response or temperature dependence, were not implemented
190 being considered minor for the multispectral instruments applied.

191 In agreement with consolidated protocols (*e.g.*, see IOCCG 2019), the impact of illumination
192 changes in profile data were minimized through normalization of each radiometric quantity with
193 respect to above–water downward irradiance $E_s(t, \lambda)$ simultaneous to the in-water measurements.
194 Specifically, the normalization aimed at producing radiometric quantities as if they were taken at
195 the same time t_0 at each depth z , where t_0 was chosen to coincide with the beginning of the
196 acquisition sequence during each cast or multi-cast.

197 The sub-surface quantities $L_u(0^-, \lambda)$, $E_u(0^-, \lambda)$ and $E_d(0^-, \lambda)$ were then determined at the
198 depth $z_0 = 0$ (identified by 0^-) as the exponentials of the intercepts resulting from the least-
199 squares linear regressions of $\ln \mathfrak{I}(z, \lambda)$ versus z within the extrapolation interval $z_0 - z_1$, where
200 $\mathfrak{I}(z, \lambda)$ indicates either $L_u(z, \lambda)$, $E_d(z, \lambda)$ or $E_u(z, \lambda)$ normalized with respect to $E_s(t, \lambda)$ at matching
201 times. The extrapolation interval was chosen on a profile-by-profile basis with the aid of
202 absorption and scattering profile data to identify the depths z_0 and z_1 , generally comprised within
203 0.3 and 5 m and best satisfying the requirement of linear decay with depth of the log-transformed
204 radiometric values. It is pointed out that the application of linear extrapolations to log-
205 transformed data to determine sub-surface radiometric values, alternative to use of non-linear
206 exponential extrapolations (see D’Alimonte et al 2012), was suggested by the objective to ensure
207 consistency with existing radiometric data datasets.

208 Extreme outliers in the $z_0 - z_1$ depth interval generally due to major wave focusing and
209 shadowing effects, were excluded from the extrapolation process by removing points exhibiting
210 distance higher than $3 \cdot \sigma$ from the linear regression line, where σ is the standard deviation of the
211 differences between data points and regression line. This filtering process is mostly effective in
212 the presence of a relatively small number of points in the extrapolation layer. The application of
213 a very slow deployment speed in the case of CoASTS radiometric data and the application of the
214 multi-cast method for BiOMaP data, ensured the availability of hundreds of measurements in
215 each selected extrapolation interval. This restricts the application of the $3 \cdot \sigma$ filter to a few
216 extreme values without significantly impacting the precision of the extrapolated data.

217 The $L_u(0^-, \lambda)$ and $E_u(0^-, \lambda)$ data products were corrected for self-shading and potential
218 bottom perturbations (Zibordi et al. 2002). Additionally, limited to CoASTS data collected in
219 the vicinity of the AAOT, corrections were also applied for perturbations due to the deployment
220 structure (Doyle and Zibordi 2002, Doyle et al. 2003). BiOMaP data, generally collected at
221 distances from the ship of approximately 15–30 m, did not require corrections for the
222 perturbations by the deployment structure.

223 In addition to $L_u(0^-, \lambda)$, $E_u(0^-, \lambda)$ and $E_d(0^-, \lambda)$, further retrieved data products are the
224 slopes of the regression fits $K_{\mathfrak{I}}(\lambda)$ (*i.e.*, $K_L(\lambda)$, $K_u(\lambda)$ and $K_d(\lambda)$) in the extrapolation interval,
225 *i.e.*, the diffuse attenuation coefficients. These $K_{\mathfrak{I}}(\lambda)$ values and particularly $K_d(\lambda)$, may exhibit
226 underestimated values due to the impact of wave focussing in the near surface water layer. This
227 effect is expected to be more pronounced for radiometric profiles collected in clear waters during
228 clear sky conditions.

229 Derived radiometric data products are then the remote sensing reflectance $R_{rs}(\lambda)$

230
231
$$R_{rs}(\lambda) = L_w(\lambda) / E_s(\lambda) \quad (1)$$

232
233 and the normalized water–leaving radiance $L_{wn}(\lambda)$

234

235
$$L_{wn}(\lambda) = R_{rs}(\lambda)E_0(\lambda), \quad (2)$$

236

237 where $E_s(\lambda)$ refers to the value measured at time t_0 , $E_0(\lambda)$ is the extra-atmospheric solar
 238 irradiance (Thuillier et al. 2003) at the mean sun-earth distance, and $L_w(\lambda)$ is the water-leaving
 239 radiance, *i.e.*, the radiance leaving the sea and quantified just above the surface through the
 240 extrapolation process, given by

241

242
$$L_w(\lambda) = 0.544 L_u(0^-, \lambda). \quad (3)$$

243

244 where the factor 0.544 accounts for the radiance reduction across the water surface due to the
 245 change in the refractive index at the air–water interface, as determined assuming that the
 246 refractive index of seawater is independent of wavelength (Austin 1974). It is acknowledged that
 247 the values of $L_w(\lambda)$ determined with Eq. 3 exhibit differences well within $\pm 1\%$ with respect to
 248 the values computed accounting for the spectral dependence of the water refractive index in the
 249 spectral range of interest (Voss and Flora 2017).

250 Finally, supplementary derived quantity is the Q -factor at nadir $Q_n(0^-, \lambda)$ determined by the
 251 ratio of $E_u(0^-, \lambda)$ to $L_u(0^-, \lambda)$ spectrally fitted to a quadratic function in the 412-555 nm spectral
 252 interval to minimize the impact of calibration and extrapolation uncertainties. The ratio of fitted
 253 $Q_n(0^-, \lambda)$ to $E_u(0^-, \lambda) / L_u(0^-, \lambda)$ provides a basic approach to evaluate the relative consistency
 254 of the $E_u(0^-, \lambda)$ and $L_u(0^-, \lambda)$ multispectral values (*e.g.*, any appreciable bias affecting a single
 255 spectral value leads to a spectral inconsistency in $E_u(0^-, \lambda) / L_u(0^-, \lambda)$).

256 The quantities $R_{rs}(\lambda)$ and $L_{wn}(\lambda)$, due to the normalization with respect to $E_s(\lambda)$, benefit of a
 257 first correction for changes in illumination conditions with sun zenith, sun-earth distance and
 258 atmospheric transmittance (Mueller and Austin 1995). The additional correction performed
 259 through the application of the $C_{f/Q}(\theta_0, \lambda, \tau_a, IOP)$ factors to $L_{wn}(\lambda)$ and analogously to $R_{rs}(\lambda)$,
 260 accounts for in-water bi-directional effects, and leads to the determination of the final $L_{WN}(\lambda)$ and
 261 $R_{RS}(\lambda)$ data products. The $C_{f/Q}$ factors are a function of the water inherent optical properties IOP
 262 (absorption and back-scattering coefficients), the atmospheric optical properties conveniently
 263 expressed through the aerosol optical depth τ_a and the sun zenith angle θ_0 . These correction
 264 factors were determined applying the tabulated values proposed by Morel et al. (2002) for Case 1
 265 waters with $IOPs$ solely expressed as a function of total chlorophyll-*a* concentration ($Chla$) as
 266 determined from water samples for each measurement station. It is acknowledged that this
 267 correction may be affected by large uncertainties when applied to optically complex waters. Still,
 268 the inclusion of both $L_w(\lambda)$ and $E_s(\lambda)$, as well as spectral values of the water inherent optical
 269 properties, would allow any potential user of the CoASTS-BiOMaP data set to implement
 270 alternative solutions for the determination of $L_{WN}(\lambda)$ and $R_{RS}(\lambda)$.

271 An estimate of the uncertainties for CoASTS and BiOMaP L_{WN} and similarly R_{RS} data, was
 272 attempted and discussed in various publications (Zibordi and Voss 2010, Zibordi et al. 2011)
 273 accounting for the major uncertainties characterizing: *i.* absolute calibration coefficients and
 274 immersion factors; *ii.* correction factors for shading perturbations; *iii.* correction factors for in-
 275 water bidirectional effects; *iv.* the determination of $E_s(\lambda)$; *v.* the quantification of $E_0(\lambda)$ when
 276 ignoring actual bandwidths; *vi.* the extrapolation process for the computation of sub-surface data;
 277 and *vii.* finally, environmental stability as a result of wave perturbations and changes in
 278 illumination conditions and seawater optical properties during profiling. In the specific case of
 279 moderate optically complex waters such as those characterizing CoASTS measurements, the
 280 uncertainties affecting L_{WN} and R_{RS} are expected to approach 5% in the blue green spectral

281 region and 7% in the red. In agreement with analyses performed for alternative *in situ*
282 radiometric methods (Gergely and Zibordi 2014), the above relative uncertainties may become
283 significantly larger in the blue spectral region for data products from marine regions
284 characterized by high water absorption such as the Baltic Sea.

285 Quality indices for radiometric products were determined during data processing in view
286 of supporting an evaluation of their accuracy. These include: *i.* the ratio $Q_R(412) = Q_n(0^-,412) /$
287 $Q_n(1,412)$ of Q_n values determined at 0^- and 1 m depths at the 412 nm center-wavelength, whose
288 significant deviation from 1 suggests issues in the extrapolation of sub-surface values; *ii.* the
289 coefficient of variation $CV_{E_s}(412)$ of in-air downward irradiance for the extrapolation interval,
290 whose high value indicates significant perturbations by ship movement or changes in
291 illumination conditions during profiling; *iii.* the diffuse to direct ratio of above-water downward
292 irradiance $R_d(412)$, whose high values indicates poor illumination conditions likely due to high
293 sun zeniths or cloudiness; *iv.* the index $R_i(412) = E_s(412) / [1.04 E_d(412)]$, whose significant
294 deviation from 1 indicates inconsistency between in-air and in-water measurements of the
295 downward irradiance; and finally *v.* the index $K_i(490)$ determined by the difference between
296 $K_d(490)$ and the corresponding value for pure water $K_w(490)$ set to 0.0212 m^{-1} (Smith and
297 Baker 1981), whose negative value identifies radiometric data products (mostly related to clear
298 waters and clear sky conditions) significantly challenged by wave perturbations.

299

300 **4.2 Absorption and attenuation from profile data**

301 Beam attenuation $c_{t-w}(z, \lambda)$ and absorption $a_{t-w}(z, \lambda)$ coefficients, excluding the contribution of
302 pure seawater, were determined from measurements performed using AC9s instruments from
303 WET Labs Inc. (Philomath, Oregon) with 25 cm path-length and nine spectral bands 10 nm wide
304 at the 412, 440, 488, 510, 555, 630, 650, 676 and 715 nm center-wavelengths. The values of
305 $c_{t-w}(z, \lambda)$ and $a_{t-w}(z, \lambda)$, in agreement with the scheme proposed by the instrument manufacturer
306 (WET Labs 2006), were corrected for the effects of differences in temperature T_w and salinity S_w
307 between field measurements and laboratory calibrations. These corrections were performed using
308 $T_w(z)$ and $S_w(z)$ profile data simultaneous to the AC9 ones.

309 AC9 absorption coefficients need correction for the non-completely reflective surfaces of
310 the absorption measurement tube, which prevents the collection of the whole scattered light and
311 naturally leads to an overestimate of $a_{t-w}(z, \lambda)$. This correction was performed by removing a
312 variable percentage of the scattering coefficient $b_{t-w}(z, \lambda)$ estimated from the difference between
313 $c_{t-w}(z, \lambda)$ and $a_{t-w}(z, \lambda)$ at each λ , assuming the absorption coefficient of particulate and dissolved
314 material is zero at the reference wavelength $\lambda_0 = 715 \text{ nm}$ and the shape of the volume scattering
315 function is spectrally independent (Zaneveld et al. 1992). Recent investigations showed this
316 correction method may lead to significant underestimates of $a_{t-w}(z, \lambda)$. Still, it was used in the
317 CoASTS-BiOMaP data processing because alternative promising correction methods such as that
318 proposed by Roettgers et al. (2013) may not be universally applicable (Stockley et al. 2017).
319 Nevertheless, the potential for applying alternative scattering corrections is allowed by including
320 in the dataset the absorption values at 715 nm, $a_{t-w}(z, 715)$, not corrected for the scattering offset
321 ($a_{t-w}(z, 715)$ would be zero when corrected).

322 The additional correction for the finite acceptance angle of the detector, which would need
323 additional field measurements of the volume scattering phase function (Boss et al. 2009) not
324 included among the CoASTS and BiOMaP core data, could not be implemented.

325 In addition to regular instrument calibration and maintenance by the manufacturer,
326 systematic AC9s pure water offsets were determined during each CoASTS campaign and at the

327 beginning and completion of each BiOMaP campaign in agreement with best practices for field
 328 operation. This offset accounts for any instrument response change while the AC9s are operated
 329 in their actual deployment configuration. The absorption and scattering offsets between the
 330 reference manufacturer calibrations and those performed in the field were applied as correction
 331 values. In the presence of appreciable offsets between successive field calibrations performed
 332 during the same campaign, differences were linearly interpolated over time.

333 Automated quality control was applied to each data record to verify the spectral and spatial
 334 (*i.e.*, vertical) consistency aiming at identifying those measurements affected by perturbations
 335 caused by bubbles or large particles flowing into the AC9 measurement chambers (*i.e.*, mostly
 336 individual spikes independently affecting $c_{t-w}(z,\lambda)$ or $a_{t-w}(z,\lambda)$ measurements especially in the
 337 surface layer). Specifically, $c_{t-w}(z,\lambda)$ and $a_{t-w}(z,\lambda)$ spectra exhibiting pronounced differences with
 338 respect to those characterizing the mean of profile spectra determined through a spectral
 339 consistency test, or pronounced changes with respect to depth at any λ identified through a
 340 spatial consistency test, were removed. The statistical parameters characterizing such a filtering
 341 process were tuned for profile data typical of individual campaigns in view of minimizing the
 342 potential for removing valid measurements.

343 The quality controlled $c_{t-w}(z,\lambda)$ and $a_{t-w}(z,\lambda)$ data were successively binned at 1 m
 344 resolution and retained when the depth d_b assigned to the center of the bin determined from the
 345 mean of the actual depths of individual measurements satisfies the condition $d_b = d_n \pm 0.25 \cdot d_i$,
 346 where d_n is the nominal depth of the center of the bin and d_i the bin width. The $c_{t-w}(\lambda)$ and
 347 $a_{t-w}(\lambda)$ values included in the CoASTS-BiOMaP dataset are the binned values tentatively
 348 corresponding to an average depth of 1 m.

349 A minimum uncertainty of 0.005 m^{-1} is assumed to affect AC9 measurements
 350 (Twardowski *et al.* 2001). Still, Stockley *et al.* (2017) showed that these values are largely
 351 underestimated especially in highly scattering waters in the blue-green spectral bands.

352

353 **4.3 Backscattering from profile data**

354 *In situ* vertical profiles of backscattering coefficients $b_b(z,\lambda)$ were determined using
 355 measurements performed with HydroScat-6 instruments from HOBI Labs Inc. (Tanque Verde,
 356 Arizona) in six bands 10 nm wide at the 442, 488, 510, 555, 620 and 676 (or 671) nm center-
 357 wavelengths. In the absence of any advanced and consolidated processing for HydroScat-6
 358 measurements, the values of $b_b(z,\lambda)$ were derived applying the conversion factor $\chi=1.08$ to
 359 measurements of the volume scattering function $\beta(z,\psi,\lambda)$ performed at the sole scattering angle
 360 $\psi=140^\circ$ (Maffione and Dana 1997). The derived backscattering values were successively
 361 corrected for the water scattering and absorption applying the factor

362

$$363 \quad \sigma_c(z, \lambda) = \exp[k_e(\lambda)(a(z, \lambda) + 0.4b(z, \lambda))] \quad (4)$$

364

365 where $a(z,\lambda)$ and $b(z,\lambda)$ (with $b(z,\lambda)=c(z,\lambda)-a(z,\lambda)$) were obtained from AC9 measurements
 366 adding the pure water absorption and scattering coefficients, respectively, while the instrument
 367 specific spectral factors $k_e(\lambda)$ were those determined by the manufacturer during the initial
 368 calibration. Salinity corrections were applied considering *Fresh water* b_{bw} from Morel (1974) for
 369 the Black Sea and Baltic Sea measurements, and the *Salt water* b_{bw} from Morel (1974) for the
 370 other measurements. This solution, with respect to the use of actual salinity values may lead to
 371 misestimates of b_{bb} generally not exceeding 2% at 443 nm for the Baltic Sea and Black Sea.

372 Equivalent to AC9 measurements, automated quality control was also applied to $b_b(z,\lambda)$
 373 data to remove measurements exhibiting poor spectral and spatial (*i.e.*, vertical) consistency (*i.e.*,
 374 mostly individual spikes affecting $b_b(z,\lambda)$ at a single λ). By tuning the parameters defining the
 375 filtering process, spectra of $b_b(z,\lambda)$ exhibiting extreme differences with respect to the mean of
 376 profile spectra, or very high changes with depth at any λ , were removed. Quality controlled
 377 $b_b(z,\lambda)$ data were also binned at 1 m resolution adopting the same criteria applied for $a(z,\lambda)$ and
 378 $c(z,\lambda)$. The $b_b(\lambda)$ values included in the CoASTS-BiOMaP dataset are the binned values
 379 tentatively corresponding to an average depth of 1 m.

380 The quality index defined by the difference between $b_b(488)$ and the corresponding value
 381 $b_{bw}(488)$ is included in the dataset to identify those measurements mostly collected in very
 382 clear waters challenged by measurement uncertainties. The values of $b_{bw}(488)$, set equal to
 383 0.001603 m^{-1} or alternatively equal to 0.001233 m^{-1} for the sole Black Sea and Baltic Sea data,
 384 were determined from those provided in Morel (1974) fitted according to Twardowski et al.
 385 (2007).

386 Annual factory calibrations performed at HOBILabs were complemented by pre-field
 387 laboratory verifications performed at the JRC Marine Optical Laboratory. These laboratory
 388 verifications aimed at correcting for HysdroScat-6 response changes between factory
 389 calibrations.

390 Whitmire et al. (2007) estimated minimum uncertainties of 0.0007 m^{-1} for measurements of
 391 $b_{bp}(z,\lambda)$ (*i.e.*, $b_b(z,\lambda)$ minus the backscattering of pure water) performed with HydroScat-6
 392 instruments. Still, also in this case, actual uncertainties are expected to be much larger.

393

394 **4.4 Absorption of particulate matter determined from discrete water samples**

395 In vivo absorption coefficients $a_p(z,\lambda)$ of aquatic particles from water samples at discrete
 396 depths z were determined using the Transmission and Reflection (*T-R*) method proposed by
 397 Tassan and Ferrari (1995). This method was shown appropriate for any particle type, including
 398 highly back-scattering mineral particles or highly absorbing sediments. The method was
 399 implemented on a Perkin Elmer Lambda-19 and from 2004 on a Lambda-950, dual beam
 400 spectrometers equipped with integrating spheres.

401 Samples of particles were collected filtering water volumes on Whatman GF/F glass fibre
 402 filters with nominal pore size of $0.7 \mu\text{m}$. Samples from the field were preserved in liquid
 403 nitrogen until laboratory analysis. The absorption coefficient $a_p(z,\lambda)$ of the equivalent particle
 404 suspension in the 400-750 nm spectral range with 1 nm resolution was determined from

405

$$406 \quad a_p(z,\lambda) = 2.3 A_s(z,\lambda) (F_a / V_w(z))^{-1} \quad (5)$$

407

408 where $V_w(z)$ is the volume of filtered water, F_a the filter clearance area and $A_s(z,\lambda)$ the equivalent
 409 particle suspension absorbance obtained with the *T-R* method.

410 The pigmented $a_{ph}(z,\lambda)$ and non-pigmented $a_{dp}(z,\lambda)$ fractions of the particulate absorption
 411 coefficient $a_p(z,\lambda)$ were obtained bleaching the sample using a solution of sodium hypochlorite
 412 (NaClO). The solution rapidly acts on pigment molecules and slowly on detritus making possible
 413 a selective analysis of the two absorption components. A description of the bleaching technique
 414 is presented in Tassan and Ferrari (1995) and in Ferrari and Tassan (1999).

415 Focused studies on the accuracy of the *T-R* method are given in Tassan and Ferrari
 416 (1995) and in Tassan et al. (2000). Still, comprehensive uncertainty estimates for $a_{ph}(z,\lambda)$ and
 417 $a_{dp}(z,\lambda)$ are not available. Nevertheless, dedicated analysis addressed the repeatability of in vivo

418 particulate absorption measurements performed with the *T-R* method (see Zibordi et al. 2002).
 419 These investigated: *i.* repeated analysis of the same sample (*i.e.*, each sample was analysed
 420 twice) and *ii.* the analysis of duplicate samples (*i.e.*, duplicates obtained from the same water
 421 volume). Results for repeated analysis of the same samples showed mean absolute percent
 422 differences of $2.9\pm 2.3\%$ at 443 nm with mean $a_p(443) = 0.082\pm 0.042 \text{ m}^{-1}$, increasing up to
 423 $7.4\pm 6.0\%$ at 555 nm with mean $a_p(555) = 0.023\pm 0.011 \text{ m}^{-1}$. These differences are attributed to: *i.*
 424 method sensitivity, and *ii.* variations in the mechanical re-positioning of the sample in front of
 425 the aperture of the integrating sphere combined with spatial non-homogeneities of the particles
 426 distribution on the filter.

427 The analysis of duplicate samples showed mean absolute percentage differences of
 428 $8.9\pm 5.9\%$ at 443 nm with mean $a_p(443) = 0.090\pm 0.049 \text{ m}^{-1}$ and of $9.8\pm 7.0\%$ at 555 nm with
 429 mean $a_p(555) = 0.024\pm 0.012 \text{ m}^{-1}$. The former differences, increased by a few percent with
 430 respect to those given for the repeated analysis of samples, are justified by: *i.* unavoidable
 431 differences in replicates due to inhomogeneity affecting the particles distributions on filters; and
 432 also *ii.* inhomogeneity in the distribution of particles in the water volumes used to produce the
 433 samples. It is mentioned that an intrinsic error in the estimate of the actual particle absorption
 434 coefficients results from the application of GF/F filters with nominal pore size of $0.7 \mu\text{m}$. In fact
 435 these filters do not allow bacteria and the fraction of mineral particles with diameter lower than
 436 $0.7 \mu\text{m}$ to be accounted for. However, the absorption of these small mineral particles is generally
 437 negligible compared to the total absorption, while the absorption of bacteria is almost 10 times
 438 lower than that of algal cells and 5–10 times lower than that of cyanobacteria (Morel and Ahn
 439 1990). The $a_{ph}(z,\lambda)$ and $a_{dp}(z,\lambda)$ measurements included in the CoASTS-BiOMaP dataset refer to
 440 water samples collected at approximately 1 m depth.

441

442 **4.5 Absorption of CDOM determined from discrete water samples**

443 The absorption coefficient $a_{ys}(z,\lambda)$ of CDOM at depth z was determined applying the
 444 method detailed in Ferrari et al. (1996) using a Perkin Elmer Lambda-12 and from 2010 a
 445 Lambda-35 dual-beam spectrometers. Samples were prepared by filtering water volumes on
 446 Millipore $0.22 \mu\text{m}$ pore size cellulose filters and adding a solution of 10 g l^{-1} of NaN_3 to the
 447 filtered water to prevent bacteria growth (typically 1 ml of the solution was added to 100 ml of
 448 filtered water).

449 CDOM samples were preserved at approximately 4°C in an amber glass bottle until
 450 laboratory analysis. The spectrometric measurements, generally carried out within a few days
 451 from the completion of the measurement campaign, were performed with 1 nm resolution in the
 452 350-750 nm spectral region. Measurements were performed placing a 10 cm quartz cuvette
 453 containing pure milli-Q water in the optical path of the reference beam, and a 10 cm quartz
 454 cuvette containing the CDOM sample in the optical path of the sample beam. It is acknowledged
 455 that the 10 cm path-length systematically applied for the analysis of CoASTS and BiOMaP field
 456 samples, naturally challenges the accuracy of measurements characterized by low CDOM
 457 absorption such as those from the Eastern Mediterranean Sea.

458 The spectral absorption coefficient $a_{ys}(z,\lambda)$ was computed from the measured absorbance
 459 $A_{ys}(z,\lambda)$ resulting from the difference between the sample absorbance and the reference
 460 absorbance (Ferrari et al., 1996), as

461

$$462 \quad a_{ys}(z,\lambda) = 2.3 A_{ys}(z,\lambda) L_c^{-1} \quad (6)$$

463

464 where L_c is the pathlength of the cuvette.

465 Assuming CDOM does not absorb in the red, the absorption coefficients are corrected for
466 the background offset by subtracting to $a_{ys}(z,\lambda)$ the mean of $a_{ys}(z,\lambda_i)$ spectral values for λ_i in the
467 670-680 nm interval.

468 Comprehensive uncertainty values are also not available for $a_{ys}(z,\lambda)$. Still, the
469 repeatability of $a_{ys}(z,\lambda)$ measurements (see Zibordi et al. 2002) was also investigated through: *i.*
470 repeated analysis of the same samples; and *ii.* the analysis of duplicate samples. The repeated
471 analysis of the same samples showed average absolute percent differences varying as a function
472 of the absorption value from $10.1\pm 7.3\%$ at 412 nm with mean $a_{ys}(z,412) = 0.168\pm 0.037 \text{ m}^{-1}$ up to
473 $24.2\pm 19.8\%$ at 555 nm with mean $a_{ys}(z,555) = 0.015\pm 0.005 \text{ m}^{-1}$. These differences are mostly
474 ascribed to the precision of the method. The analysis of the duplicate samples showed expected
475 augmented average absolute percent differences when compared to repeated analysis of samples
476 varying from $12.1\pm 6.3\%$ at 412 nm with mean $a_{ys}(z,412) = 0.175\pm 0.038 \text{ m}^{-1}$ and up to
477 $30.3\pm 23.8\%$ at 555 nm with mean $a_{ys}(z,555) = 0.018\pm 0.005 \text{ m}^{-1}$. The latter increased values are
478 largely justified by differences between samples.

479 It is finally mentioned that the use of $0.22 \mu\text{m}$ pore size filters to produce CDOM
480 samples, when the $0.7 \mu\text{m}$ pore size filters are applied for the quantification of particle
481 absorption coefficients, suggests that the overall absorption budget cannot be fully resolved. In
482 fact, as already anticipated, bacteria and very small mineral particles having size between 0.2 and
483 $0.7 \mu\text{m}$, are not included in the absorption analysis. Still, this missing contribution to the overall
484 absorption budget is expected to be minor.

485 As per $a_{ph}(\lambda)$ and $a_{dp}(\lambda)$, also the $a_{ys}(\lambda)$ measurements included in the CoASTS-BiOMaP
486 dataset refer to water samples collected at approximately 1 m depth.

487

488 **4.6 Pigments concentration**

489 Phytoplankton pigment concentrations were determined by using High Performance Liquid
490 Chromatography (HPLC) with the method proposed by Van Heukelem and Thomas (2005).
491 Exceptions are the samples collected before 2000 for which the method proposed by Jeffrey et al.
492 (1997) was applied.

493 The analysis were performed on samples of particulate matter retained on GF/F filters with a
494 nominal pore size of $0.7\mu\text{m}$: this choice is justified by the diameter of living phytoplankton cells
495 generally higher than $1 \mu\text{m}$ (Stramsky and Kiefer, 1991). After filtration, samples were preserved
496 in liquid nitrogen until laboratory analysis.

497 Following Van Heukelem and Thomas (2005), the samples were transferred to vials with 3
498 ml 95% acetone and vitamin E as internal standard. Samples were then disrupted using a vortex
499 mixer, sonicated on ice, extracted at 4°C for 20 h, and mixed again. The samples were
500 successively filtered through $0.2 \mu\text{m}$ Teflon syringe filter into HPLC vials and placed in the
501 cooling rack of the HPLC system. Buffer and sample were injected in the HPLC (Shimadzu LC-
502 10A or alternatively an HP-1100, systems) in the 5/2 ratio using a pre-treatment program and
503 mixing in the loop before injection.

504 The list of pigments systematically analysed at the JRC Marine Optical Laboratory or
505 alternatively at DHI A/S (Hørsholm, Denmark) includes: chlorophyll a (resulting from the sum
506 of divinyl- and monovinyl-chlorophyll a), chlorophyll b, chlorophyll c_1+c_2 , chlorophyllide a,
507 fucoxanthin, diadinoxanthin, β -carotene, zeaxanthin, alloxanthin, 19'-butanoyloxyfucoxanthin,
508 19'-hexanoyloxyfucoxanthin and diatoxanthin.

509 Various inter-comparisons of HPLC methods performed within the framework SeaWiFS
510 HPLC Analysis Round-Robin Experiments (SeaHARRE) organized by NASA with the JRC
511 participation, demonstrated the capability of various laboratories to achieve differences lower
512 than 6% in the determination of total chlorophyll *a* concentration *Chla* (*i.e.*, the sum of
513 chlorophyll *a* and chlorophyllide *a*) and lower than 25% for the other ancillary pigments
514 characterizing marine waters (Hooker et al. 2010). The analysis of CoASTS and BiOMaP shows
515 *Chla* values always higher than 0.03 - 0.04 $\mu\text{g l}^{-1}$. This may suggest some quantification limit for
516 the methodology applied to determine pigments concentration.

517 Consistent with $a_{\text{ph}}(z,\lambda)$, $a_{\text{dp}}(z,\lambda)$ and $a_{\text{ys}}(z,\lambda)$, measurements of *Chla* were performed on
518 water samples collected at approximately 1 m depth.

519

520 **4.7 Suspended particulate concentration**

521 The concentration of suspended particulate matter, *SPM*, was obtained from the net weight
522 of the particulate material collected on filters following the method detailed in Van der Linde
523 (1998) as an evolution of that proposed by Strickland and Parsons (1972). Samples were
524 produced by filtering volumes of water on GF/F filters with 0.7 μm nominal pore size previously
525 baked at 450 $^{\circ}\text{C}$ for 1 hour, pre-washed, dried for 1 hour at 75 $^{\circ}\text{C}$ and finally pre-weighed on a
526 electrobalance. After water filtration, the filters (*i.e.*, filtration area and border) were washed
527 with distilled water and stored at -18 $^{\circ}\text{C}$ for successive laboratory analysis. Before final
528 weighting, the filters were dried at 75 $^{\circ}\text{C}$ for 1 hour, and then temporarily stored in a desiccator.

529 The concentration of *SPM* was calculated from

530

$$531 \quad SPM(z) = [(W_f(z) - W_s(z)) - w_b] V(z)^{-1} \quad (7)$$

532

533 where $W_f(z)$ is the weight of the filter before filtration, $W_s(z)$ is the weight of the filter after
534 filtration, $V(z)$ is the volume of the filtered water and w_b is a correction term introduced to
535 account for variations in the weight of the filter sample due to changes in environmental
536 conditions between the two weightings steps. The values of w_b were determined from *blank*
537 filters (*i.e.*, GF/F filters completely conditioned, not used for water filtration, but exposed to the
538 same processes of the sample filters: transportation to the measurement site and back, storage in
539 the freezer, drying). The w_b values applied in Eq. 7, are the differences between the average final
540 weight of *blank* filters and their original average weight.

541 *SPM* values included in the CoASTS-BiOMaP data set are generally obtained from the
542 average of duplicate samples. In the case of large differences between duplicates (*i.e.*, tentatively
543 exceeding 20%) the *SPM* value from one of the two samples is used prior investigating the
544 surface and integrity of the samples, and also verifying the consistency of their values with AC9
545 measurements from close stations.

546 The use of GF/F filters with 0.7 μm nominal pore size for *SPM* analysis leads to an
547 underestimate of total suspended matter due to the loss of particles with diameter lower than 0.7
548 μm . However, it is recognized that the filter rinsing for salt removal and the filter conditioning
549 after filtration before final weighting, can induce errors certainly much larger than the mass of
550 particles with diameter lower than 0.7 μm .

551 An analysis of measurement repeatability performed with duplicate samples showed mean
552 percent difference equal to 13.9 \pm 13.4% with mean $SPM(z) = 0.86\pm 0.40 \text{ mg}\cdot\text{l}^{-1}$. The largest
553 differences between duplicate samples (*i.e.*, larger than 30%) were observed with values of

554 $SPM(z)$ lower than approximately 0.5 mg l^{-1} . This is explained by the intrinsic uncertainty
555 affecting sample preparation (*i.e.*, water sample non-homogeneity and filter rinsing).

556 As for other quantities determined from the analysis of water samples, also the SPM values
557 included in the CoASTS-BiOMaP dataset refer to samples collected at approximately 1 m depth.

558

559 **4.8 Salinity and temperature**

560 Profiles of salinity $S_w(z)$ and temperature $T_w(z)$ measurement were performed with SBE
561 19-plus Conductivity-Temperature-Depth (CTD) sensors from Sea-Bird Scientific (Bellevue,
562 Washington). These devices were calibrated by the manufacturer approximately on a two-year
563 basis. Uncertainties are tentatively expected to be within 0.01‰ for salinity and 0.01°C for
564 temperature.

565 Equivalent to $a(z,\lambda)$, $c(z,\lambda)$ and $b_b(z,\lambda)$ profiles, automated quality control was also
566 applied to $S_w(z)$ and $T_w(z)$ data to remove measurement artefacts. By trimming filtering parameters
567 to individual campaigns, values of $S_w(z)$ and $T_w(z)$ exhibiting extreme changes with respect to
568 depth, were removed. Quality checked $S_w(z)$ and $T_w(z)$ data were binned at 1 m resolution
569 adopting the same criteria already applied for $a(z,\lambda)$, $c(z,\lambda)$ and $b_b(z,\lambda)$. The values associated
570 with the first bin, tentatively representing the 1 m depth, are included in the CoASTS-BiOMaP
571 dataset.

572

573 **4.9 Meteorological and environmental observations**

574 Among the meteorological quantities and observations recorded during each measurement
575 station, the wind speed W_s , sea state S_s and cloud cover C_c are included in the data set.

576

577 **5. The near-surface CoASTS and BiOMaP dataset (CoASTS-BiOMaP)**

578 CoASTS-BiOMaP data are accessible at <https://doi.org/10.1594/PANGAEA.971945> in
579 tabular form and include the near-surface data products from CoASTS and BiOMaP
580 measurements of relevance for the validation of satellite ocean color data and the development of
581 bio-optical algorithms. All spectral data products are restricted to the nominal center-
582 wavelengths 412, 443, 490, 510, 555, 665 nm, unless diversely specified. CoASTS data products
583 are only provided from December 1998 when full standardization of measurements and
584 processing was put in place. In addition, station data were excluded from CoASTS-BiOMaP
585 when the $L_{WN}(\lambda)$ or $K_d(\lambda)$ radiometric products did not satisfy basic quality control criteria by
586 exhibiting spectra with unexplained shape or amplitude. Furthermore, poor quality of data
587 products other than radiometric, implied the exclusion of their individual values from the dataset.

588 Table 3 provides a comprehensive list of the quantities included in the CoASTS-BiOMaP
589 dataset: each one is identified by a convenient symbol, a brief description and its physical units.
590 A summary of the average values of the major bio-optical and hydrographic quantities
591 determined for the various marine regions is provided in Table 4. These are: the diffuse
592 attenuation coefficient K_d at 490 nm, the water absorption coefficient (from discrete sample
593 analysis, pure water contribution excluded) a at 490 nm, the backscattering coefficient (water
594 contribution included) b_b at 488 nm; the concentrations of total chlorophyll-a $Chla$ and
595 suspended particulate matter SPM ; and the salinity S_w . All quantities exhibit ample differences
596 across the various marine regions. Notable, variations in $K_d(490)$ exceed one order of magnitude
597 between the Eastern Mediterranean (EMED) and the Baltic Sea (BLTS) waters (*i.e.*, $K_d(490)$
598 varies from 0.037 to 0.494 m^{-1}).

599 Figure 3 displays BioMaP and CoASTS $L_{WN}(\lambda)$ spectra for the different marine regions.
600 These spectra clearly indicate diverse bio-optical features for the different regions. They span
601 from the highly oligotrophic Eastern Mediterranean Sea (EMED) showing maximum values in
602 the blue region, to the optically complex Baltic Sea (BLTS) dominated by the presence of high
603 concentrations of CDOM as expressed by low values of L_{WN} in the blue spectral region. Between
604 these, there are marine regions exhibiting diverse bio-optical complexity due to different
605 concentration of optically significant constituents. Notably, some spectra from the North Sea
606 (NORS) indicate the presence of relatively high concentration of sediments, while spectra from
607 the Black Sea (BLK) and the northern Adriatic Sea (AAOT) suggest bio-optical conditions
608 determined by the presence of various concentrations of SPM and CDOM determining L_{WN}
609 maxima at the 510 or 555 nm center-wavelengths.

610 Table 5 provides the mean spectral values and related standard deviations of $Q_n(\lambda)$ for the
611 various marine regions as determined from radiometric profiles performed during near clear sky
612 conditions determined by $C_c \leq 1/4$. These naturally exhibit some spectral dependence varying
613 with the water type. For instance, $Q_n(\lambda)$ from the Eastern Mediterranean Sea (EMED) exhibit
614 almost spectrally constant mean values approaching 4 sr in the 412-555 nm spectral interval and
615 of approximately 5 sr at 665 nm. Conversely, regions such as the northern Adriatic Sea (AAOT)
616 exhibit mean values approaching 4.5 sr with some spectral dependence in the 412-555 nm
617 spectral region, and also a mean value of 5 sr at 665 nm.

618 Figure 4 displays the $a_{ph}(\lambda)$ spectra for the CoASTS and BioMaP regions. Notable is the
619 increase in the values of mean $a_{ph}(443)$ from 0.007 m^{-1} for the Eastern Mediterranean Sea
620 (EMED) to 0.191 m^{-1} and 0.220 m^{-1} for the Baltic Sea (BLTS) and North Sea (NORS),
621 respectively. The peculiar spectra shown by North Sea stations off the Belgian coast exhibiting
622 a_{ph} values higher at 412 nm than at 443 nm (see panel for NORS data in Fig. 4), are explained by
623 high concentrations of pheophytin leading to an increase of the absorption coefficient toward 412
624 nm.

625 Figure 5 displays the comparison of the near surface absorption coefficients (pure water
626 excluded) determined from AC9 measurements at the center-wavelength of 443 nm, $a_{t-w}(AC9)$,
627 versus the equivalent absorption coefficients determined from water samples, $a_{t-w}(\text{sample}) =$
628 $a_{ph}(443) + a_{dt}(443) + a_{ys}(443)$. Results suggest an increasing underestimate of $a_{t-w}(AC9)$ and larger
629 relative scattering with a decrease in absorption. This is highlighted by the scatter plots of data
630 from the Eastern Mediterranean Sea (EMED) exhibiting an underestimate exceeding 70% with
631 values of $a_{t-w}(\text{samples})$ generally lower than 0.1 m^{-1} . Conversely, the Baltic Sea (BLTS) shows
632 outstanding agreement between the compared quantities with absorption values comprised in the
633 range of $0.2\text{-}1.2 \text{ m}^{-1}$. These mean differences between $a_{t-w}(AC9)$ and $a_{t-w}(\text{samples})$ absorption
634 values could be explained by an incomplete correction of the perturbing effects due to finite
635 acceptance angle of the detector, the non-fully reflective surface of the AC9 absorption chamber
636 (*i.e.*, the two short 25 cm path-length tubes) and also by the non-negligible absorption of
637 particles at the reference wavelength $\lambda_0 = 715 \text{ nm}$ applied for scattering corrections.

638
639
640
641
642
643

644 Table 3. The CoASTS-BiOMaP data set: quantities identified by symbols, description of
645 quantities and related units.

| Symbol | Description | Units | Details |
|--------------------------|--------------------------------------------------------------------------------------------------------------------------------------------------------|----------------------------|------------------------------------------------------------------------------------------------------------------------------------------------------|
| <i>Station ID</i> | Station identifier | Code | <i>Gcessit</i> ⁽¹⁾ |
| <i>Date&Time</i> | Date and time | GMT | <i>yyyy-mm-ddT hh:mm:ss</i> ⁽²⁾ |
| <i>Lon</i> | Longitude | Degrees | |
| <i>Lat</i> | Latitude | Degrees | |
| <i>Sz</i> | Sun zenith | Degrees | |
| <i>Sa</i> | Sun azimuth | Degrees | |
| $L_u(\lambda)$ | Upwelling radiance at depth 0 ⁻ | $W m^{-2} nm^{-1} sr^{-1}$ | At nominal λ_s ⁽³⁾ |
| $E_d(\lambda)$ | Downward irradiance at depth 0 ⁻ | $W m^{-2} nm^{-1}$ | At nominal λ_s ⁽³⁾ |
| $E_u(\lambda)$ | Upward irradiance at depth 0 ⁻ | $W m^{-2} nm^{-1}$ | At nominal λ_s ⁽³⁾ |
| $K_L(\lambda)$ | Diffuse att. coeff. from $L_u(z,\lambda)$ | m^{-1} | At nominal λ_s ⁽³⁾ |
| $K_d(\lambda)$ | Diffuse att. coeff. from $E_d(z,\lambda)$ | m^{-1} | At nominal λ_s ⁽³⁾ |
| $K_u(\lambda)$ | Diffuse att. coeff. from $E_u(z,\lambda)$ | m^{-1} | At nominal λ_s ⁽³⁾ |
| $E_s(\lambda)$ | Downward irradiance at depth 0 ⁺ | $W m^{-2} nm^{-1}$ | At nominal λ_s ⁽³⁾ |
| $Q_n(\lambda)$ | Q -factor an nadir at depth 0 ⁻ | sr | At nominal λ_s ⁽³⁾ |
| $R_{RS}(\lambda)$ | Remote sensing reflectance at depth 0 ⁺ | sr^{-1} | At nominal λ_s ⁽³⁾ |
| $L_{WN}(\lambda)$ | Normalized water-leaving rad. at depth 0 ⁺ | $W m^{-2} nm^{-1} sr^{-1}$ | At nominal λ_s ⁽³⁾ |
| $Q_R(412)$ | Ratio of $Q_n(412)$ at depth 0 ⁻ to $Q_n(1,412)$ at 1 m depth | – | Introduced to best support the use of $Q_n(\lambda)$ (large deviations from 1 may indicate extrapolation issues) |
| $R_d(412)$ | Ratio of the diffuse $E_i(412)$ to direct [$E_s(412) - E_i(412)$] above-water downward irradiance at 412 nm | – | |
| $CV E_s(412)$ | Coefficient of variation $E_s(412)$ | % | |
| $R_i(412)$ | Ratio of the above-water downward irradiance $E_s(412)$ to the in-water downward irradiance $E_d(412)$ multiplied by 1.04 | – | |
| $K_i(490)$ | Diffuse attenuation coefficient $K_d(490)$ minus the diffuse attenuation coefficient of pure sea water $K_w(490)$ assumed constant and equal to 0.0212 | m^{-1} | Introduced to best support the exploitation of data (a negative value may suggest extrapolation challenged by wave perturbations) |
| $a_{ph}(\lambda)$ | Absorption coefficient by pigmented particles at 1 m depth | m^{-1} | At nominal λ_s ⁽³⁾ |
| $a_{dt}(\lambda)$ | Absorption coefficient by non-pigmented part. at 1 m depth | m^{-1} | At nominal λ_s ⁽³⁾ |
| $a_{ys}(\lambda)$ | Absorption coefficient by CDOM at 1 m depth | m^{-1} | At nominal λ_s ⁽³⁾ |
| $a_{t-w}(\lambda)$ | Absorption coefficient from AC9 at 1 m depth | m^{-1} | At AC9 λ_s ⁽⁴⁾ . The values $a_{t-w}(715)$ are not corrected for the scattering offset. If corrected, their values would be zero. |
| $c_{t-w}(\lambda)$ | Beam attenuation coefficient from AC9 at 1 m depth | m^{-1} | At AC9 λ_s ⁽⁴⁾ |
| $b_b(\lambda)$ | Backscattering coefficient from HydroScat-6 at 1 m depth | m^{-1} | At HydroScat-6 λ_s ⁽⁵⁾ |
| $b_b(488) - b_{bw}(488)$ | Backscattering coefficient $b_b(488)$ minus | m^{-1} | Introduced to best support the |

| | | | |
|-------------|----------------------------------------------------------------------------------------------------------------------------------------------------------------------------------------------------------------------|----------------------|-----------------------------------------------------------------------------------------------------------|
| | the backscattering coefficient of pure sea water $b_{bw}(488)$ assumed constant and equal to 0.001603 m^{-1} or alternatively 0.001233 m^{-1} for the sole Black Sea and Baltic Sea measurements | | exploitation of data (a negative value may indicate measurements challenged by significant uncertainties) |
| <i>Chla</i> | Total chlorophyll- <i>a</i> concentration at 1 m depth ⁽⁶⁾ | $\mu\text{g l}^{-1}$ | |
| <i>SPM</i> | Suspended particulate matter concentration at 1 m depth | mg l^{-1} | |
| T_w | Temperature of seawater at 1 m depth | $^{\circ}\text{C}$ | |
| S_w | Salinity of seawater at 1 m depth | ‰ | |
| W_s | Wind speed | m s^{-1} | |
| S_s | Sea state | 0-9 | WMO scale |
| C_c | Cloud cover | 0-4 | Octa/2 |

646 ¹ *G* indicates the site or geographic region (*V* and *W* for AAOT, *A* for Adriatic Sea, *B* for Baltic Sea, *E* for Eastern
647 Mediterranean Sea, *K* for Black Sea, *L* for Ligurian Sea, *N* for North Sea, *O* for Western Mediterranean Sea, *I* for
648 Iberian Shelf, *P* for Greenland Sea), while *cc* indicates the campaign number for the specific region, *ss* the station
649 number and *ii* the cast number.

650 ² The letters *yyyy* indicate the year, *mm* the month, *dd* the day *hh*, the hours and *mm* the minutes.

651 ³ Nominal center-wavelengths for radiometric data products are 412, 443, 490, 510, 555 are 665 nm.

652 ⁴ Center-wavelengths for AC9 data products are 412, 440, 488, 510, 555, 630, 650, 676, and 715 nm.

653 ⁵ Center-wavelengths for HydroScat-6 data products are 442, 488, 510, 555, 620, and 676 (or 671) nm.

654 ⁶ Total chlorophyll-*a* concentration indicates the sum of chlorophyllide-*a*, monovinyl- and divinyl-chlorophyll-*a*.

655

656

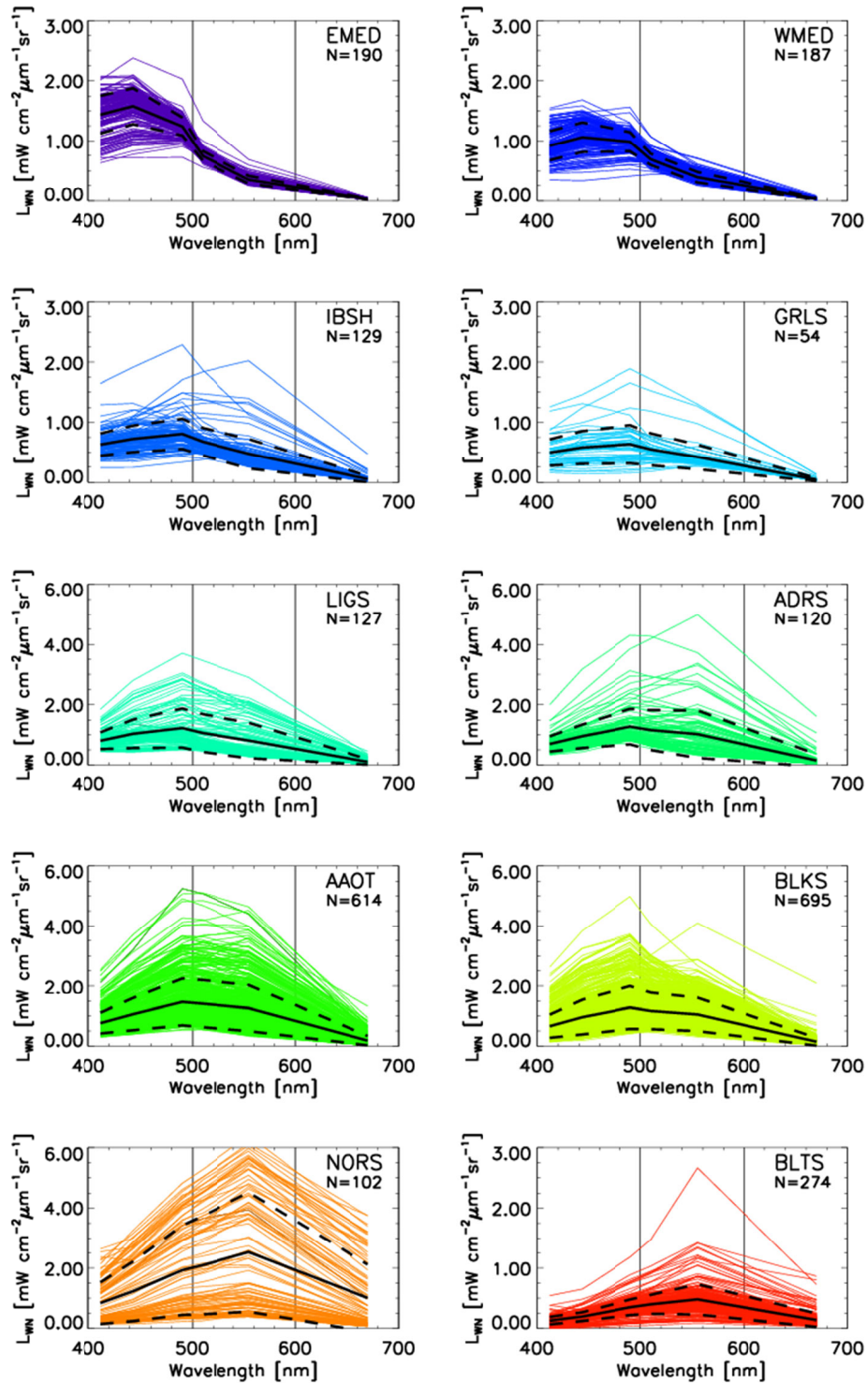
657 Table 4. Mean \pm standard deviations of quantities describing the bio-optical and hydrographic
658 characteristics of the CoASTS and BioMaP marine regions: the diffuse attenuation coefficient K_d
659 at 490 nm; the seawater absorption coefficient (excluding pure water contribution) a determined
660 from discrete sample analysis at 490 nm; the backscattering coefficient (including pure water
661 contribution) b_b at 488 nm; the concentrations of total chlorophyll-*a* *Chla* and suspended
662 particulate matter *SPM*; and finally the salinity S_w .

663

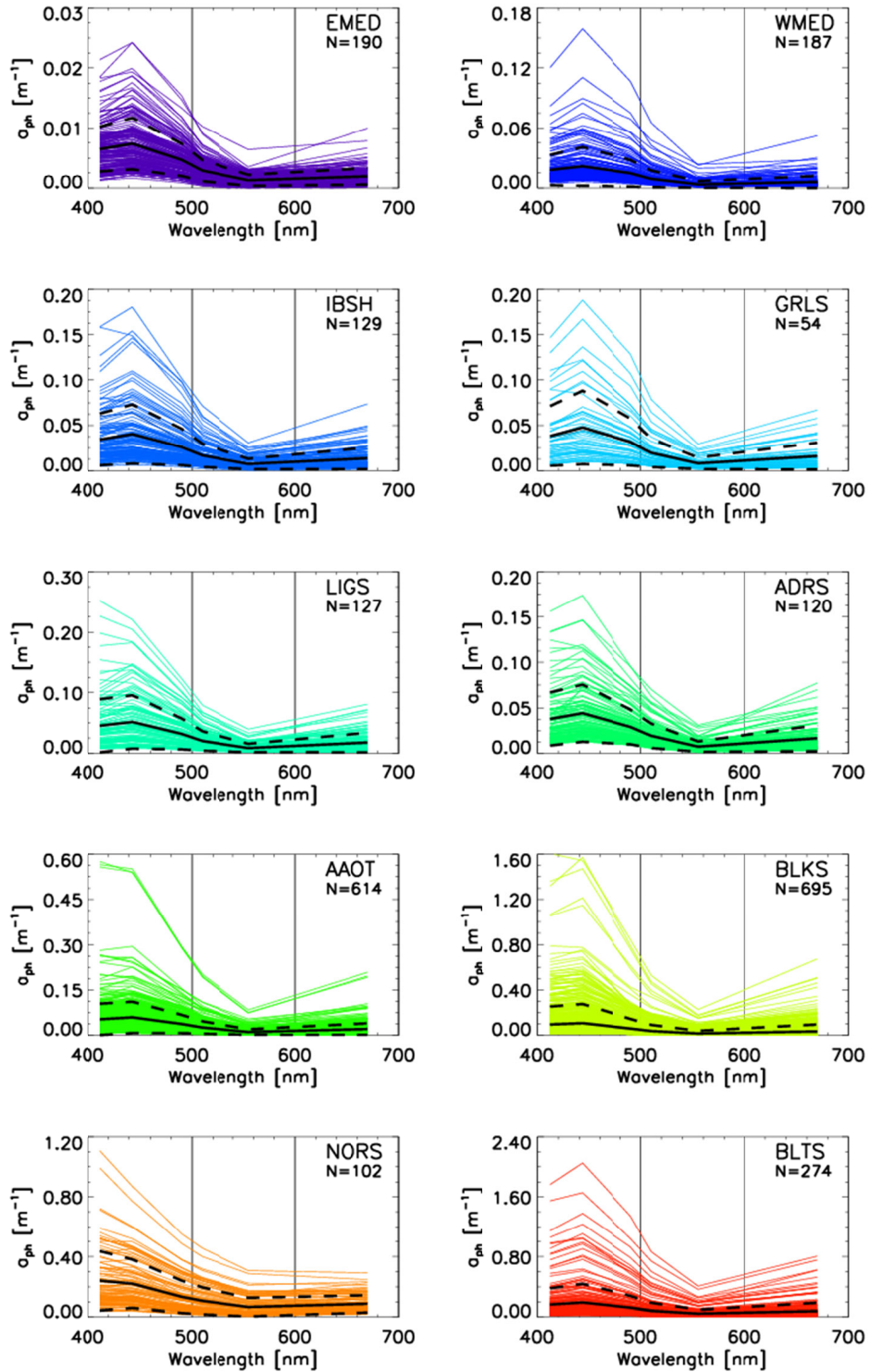
| Region | $K_d(490)[\text{m}^{-1}]$ | $a(490) [\text{m}^{-1}]$ | $b_b(488)[\text{m}^{-1}]$ | <i>Chla</i> $[\mu\text{g l}^{-1}]$ | <i>SPM</i> $[\text{mg l}^{-1}]$ | $S_w[\text{‰}]$ |
|--------|---------------------------|--------------------------|---------------------------|------------------------------------|---------------------------------|-----------------|
| EMED | 0.037 \pm 0.022 | 0.031 \pm 0.012 | 0.0026 \pm 0.0007 | 0.09 \pm 0.08 | 0.27 \pm 0.45 | 38.6 \pm 0.7 |
| WMED | 0.046 \pm 0.025 | 0.040 \pm 0.019 | 0.0032 \pm 0.0009 | 0.30 \pm 0.37 | 0.30 \pm 0.22 | 37.8 \pm 0.4 |
| IBSH | 0.084 \pm 0.049 | 0.073 \pm 0.033 | 0.0040 \pm 0.0023 | 0.81 \pm 0.83 | 0.53 \pm 0.39 | 36.0 \pm 0.2 |
| GRLS | 0.097 \pm 0.062 | 0.082 \pm 0.032 | 0.0039 \pm 0.0021 | 0.94 \pm 1.04 | 0.64 \pm 0.28 | 34.0 \pm 1.6 |
| LIGS | 0.110 \pm 0.079 | 0.079 \pm 0.045 | 0.0078 \pm 0.0067 | 0.93 \pm 0.85 | 0.71 \pm 0.57 | 37.7 \pm 1.0 |
| ADRS | 0.141 \pm 0.125 | 0.085 \pm 0.059 | 0.0090 \pm 0.0067 | 1.25 \pm 1.32 | 1.14 \pm 1.45 | 35.6 \pm 2.3 |
| AAOT | 0.176 \pm 0.102 | 0.099 \pm 0.053 | 0.0121 \pm 0.0073 | 1.28 \pm 1.13 | 1.25 \pm 0.76 | 34.9 \pm 2.3 |
| BLKS | 0.219 \pm 0.254 | 0.131 \pm 0.130 | 0.0093 \pm 0.0066 | 1.62 \pm 3.13 | 1.17 \pm 1.24 | 16.6 \pm 1.8 |
| NORS | 0.876 \pm 0.864 | 0.377 \pm 0.346 | 0.0197 \pm 0.0160 | 4.23 \pm 2.27 | 9.96 \pm 12.52 | 33.7 \pm 1.4 |
| BLTS | 0.494 \pm 0.409 | 0.308 \pm 0.269 | 0.0107 \pm 0.0084 | 4.99 \pm 8.04 | 1.53 \pm 1.71 | 6.2 \pm 1.4 |

664

665

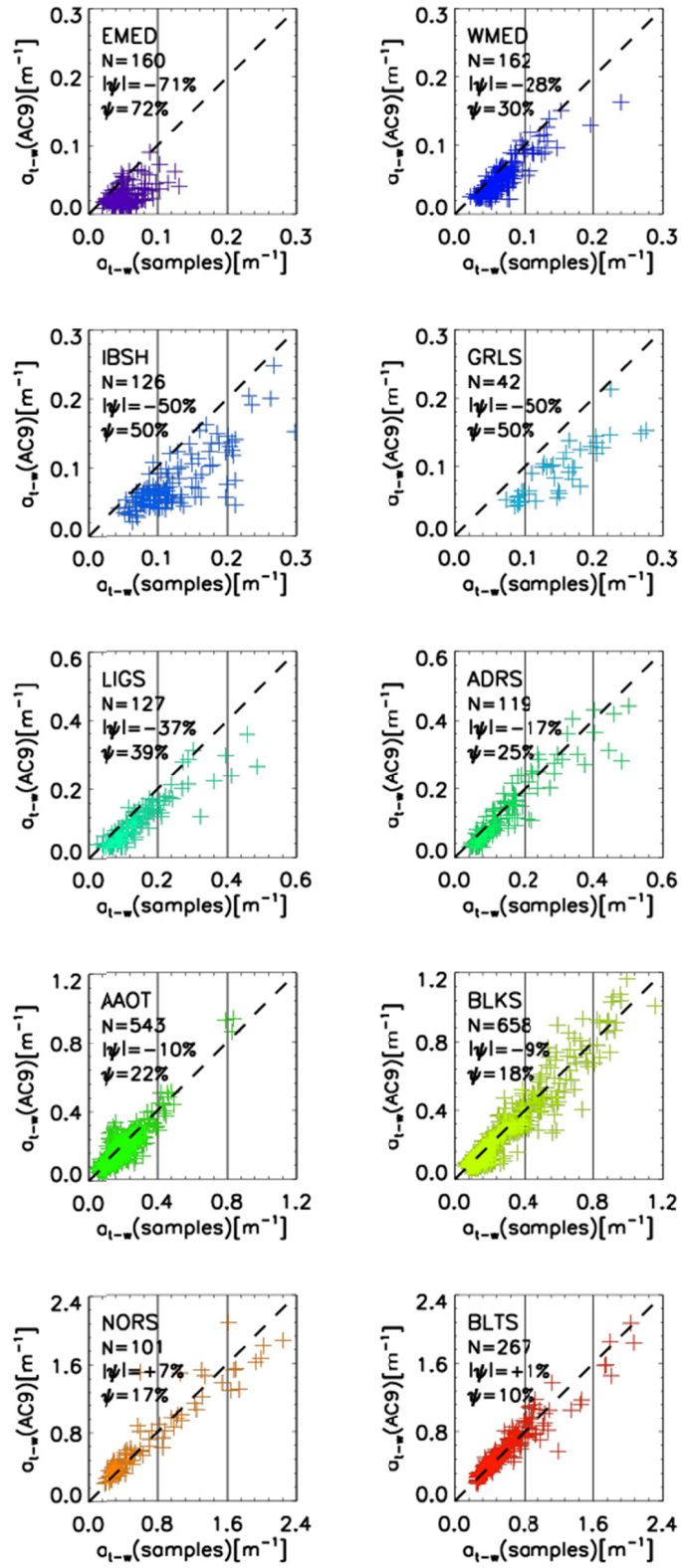


666
 667 Figure 3. Spectra of $L_{WN}(\lambda)$ for the CoASTS and BioMaP geographic regions (see Table 1 for
 668 acronyms). N indicates the number of spectra. The continuous black lines indicate mean values
 669 while the dashed lines indicate ± 1 standard deviation. For convenience, the spectra are plotted in
 670 units of $\text{mW cm}^{-2} \mu\text{m}^{-1} \text{sr}^{-1}$.



671

672 Figure 4. Spectra of $a_{ph}(\lambda)$ for the CoASTS and BioMaP marine regions. N indicates the number
 673 of spectra. The continuous black lines indicate mean values while the dashed lines indicate ± 1
 674 standard deviation.



675
676

677 Figure 5. Scatter plot of AC9 derived $a_{t-w}(AC9)$ and laboratory measurements performed on
 678 water samples $a_{t-w}(\text{samples})$, of the water absorption coefficient (water excluded) determined at
 679 the 443 nm center-wavelength for the diverse CoASTS and BioMaP marine regions. N indicates
 680 the number of samples while $|\psi|$ and ψ indicate the mean of absolute (unsigned) percent
 681 differences and the mean of (signed) percent differences, respectively.

682
 683

684 Table 5. Spectral values of $Q_n(\lambda)$ in units of sr at the 412, 443, 490, 510, 555 and 670 nm center-
 685 wavelengths for the CoASTS and BioMaP marine regions, determined from in-water radiometric
 686 profiles performed with cloud cover $C_C \leq 1/4$.

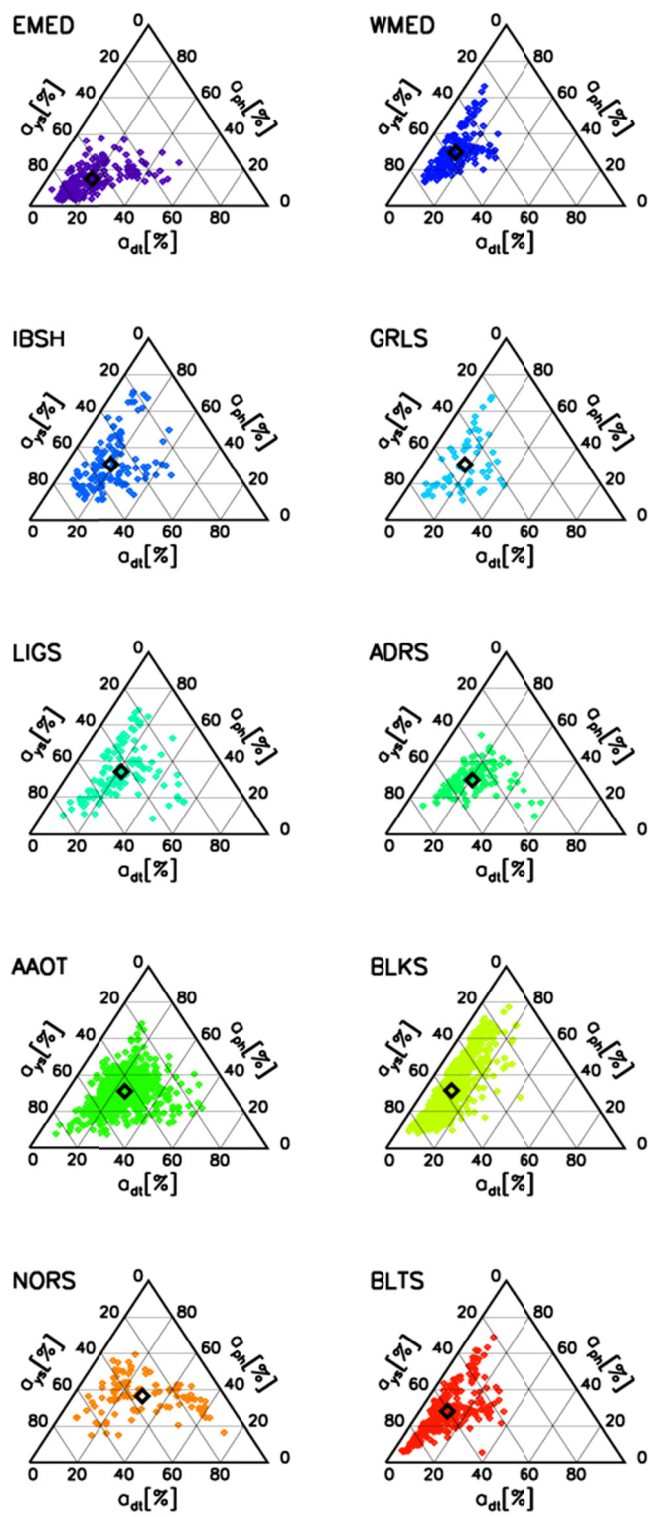
| Region | 412 | 443 | 490 | 510 | 555 | 670 |
|--------------|-----------|-----------|-----------|-----------|-----------|-----------|
| EMED (N=127) | 3.89±0.33 | 3.90±0.36 | 3.88±0.42 | 3.87±0.45 | 3.84±0.54 | 4.90±1.12 |
| WMED (N=100) | 4.08±0.36 | 4.14±0.41 | 4.20±0.46 | 4.21±0.48 | 4.19±0.52 | 4.96±0.76 |
| IBSH (N=87) | 4.18±0.37 | 4.22±0.38 | 4.26±0.43 | 4.26±0.45 | 4.24±0.51 | 4.58±0.59 |
| GRLS (N=11) | 3.97±0.33 | 4.08±0.37 | 4.14±0.38 | 4.12±0.37 | 4.00±0.34 | 4.18±0.38 |
| LIGS (N=53) | 4.52±0.40 | 4.54±0.36 | 4.57±0.36 | 4.59±0.38 | 4.66±0.44 | 5.14±0.58 |
| ADRS (N=71) | 4.47±0.65 | 4.39±0.57 | 4.33±0.54 | 4.34±0.55 | 4.40±0.62 | 4.98±0.95 |
| AAOT (N=372) | 4.56±0.56 | 4.43±0.51 | 4.33±0.49 | 4.33±0.50 | 4.41±0.58 | 5.02±0.84 |
| BLKS (N=401) | 4.51±0.54 | 4.49±0.57 | 4.47±0.59 | 4.47±0.59 | 4.47±0.59 | 5.06±0.80 |
| NORS (N=27) | 4.70±0.60 | 4.71±0.57 | 4.69±0.54 | 4.67±0.53 | 4.60±0.50 | 4.90±0.48 |
| BLTS (N=87) | 4.93±0.69 | 5.09±0.74 | 5.18±0.78 | 5.16±0.76 | 4.99±0.66 | 5.20±0.86 |

687
 688

689 Figure 6 shows trilinear (ternary) plots of the absorption coefficients $a_{ys}(443)$, $a_{dt}(443)$ and
 690 $a_{ph}(443)$, expressed in percent of the total absorption (*i.e.*, with respect to $a_{ys}(443)+a_{dt}(443)+$
 691 $a_{ph}(443)$), displayed with values increasing in the counter-clockwise direction (Harris 1999).
 692 These results exhibit very few cases characterized by dominance of absorption by particles with
 693 a_{ph} and a_{dt} values close to the upper and lower right apexes, respectively. Conversely, most of the
 694 cases indicate dominance of absorption by coloured dissolved organic matter: see the a_{ys} values
 695 near the lower left apex). This is particularly evident for the oligotrophic waters of the Eastern
 696 Mediterranean Sea (EMED), and by the patterns characterizing the oligotrophic-mesotrophic
 697 waters of the Western Mediterranean Sea (WMED), the optically complex water of the Black
 698 Sea (BLKS) and the highly absorbing waters of the Baltic Sea (BLTS).

699 The specific results shown for the Mediterranean Sea (*i.e.*, EMED and WMED), which
 700 may suggest inconsistency with the definition of Case-1 waters (IOCCG 2000), are supported by
 701 an independent study from Pérez et al. (2016).

702



703
 704 Figure 6. Trilinear (ternary) plots of the absorption coefficients a_{ys} , a_{dt} and a_{ph} expressed in
 705 percent of the total absorption (*i.e.*, with respect to $a_{ys}+a_{dt}+a_{ph}$) at the 443 nm center-wavelength.
 706 The empty black square indicates the mean of the plotted values.

707 Parameters determined from the exponential fit versus wavelength of $a_{dt}(\lambda)$ and $a_{ys}(\lambda)$, and
 708 the power law fit of $b_b(\lambda)$ versus wavelength, are provided in Tables 6-8. Specifically, the
 709 spectral values of $a_{dt}(\lambda)$ and $a_{ys}(\lambda)$ were fitted within the 412-665 nm spectral interval using

$$710 \quad a_{dt}(\lambda) = A_{dt} \exp(-S_{dt}(\lambda - 412)) + B_{dt} \quad (8)$$

711 and

$$712 \quad a_{ys}(\lambda) = A_{ys} \exp(-S_{ys}(\lambda - 412)) + B_{ys}, \quad (9)$$

713 where A_{dt} and A_{ys} indicate the absorption coefficients fitted at 412 nm, S_{dt} and S_{ys} the slope of
 714 the exponential function, and, B_{dt} and B_{ys} account for the background.

715 Conversely, the spectral values of $b_b(\lambda)$ at the center-wavelengths $\lambda=442, 488, 510, 550$ and
 716 620 nm (excluding 676 or 6171 nm due to potential perturbations by fluorescence), were fitted
 717 using

$$718 \quad b_b(\lambda) = A_b (\lambda/442)^{-S_b}, \quad (10)$$

719 where A_b indicates the backscattering coefficient at 442 nm and S_b the slope of the power law
 720 function.

721 Table 6 shows mean values of the slope S_{dt} varying from 0.009 nm^{-1} for the Eastern
 722 Mediterranean Sea (EMED) up to 0.013 for the North Sea (NORS). Values of the bias B_{dt}
 723 naturally increase with A_{dt} : the largest value of $B_{dt} = 0.067 \text{ m}^{-1}$ is observed for the North Sea
 724 (NORS) that also exhibits the highest value of $A_{dt} = 0.288 \text{ m}^{-1}$. Residuals R_{dt} , which also
 725 increase with A_{dt} , are quite minor suggesting a general good performance of the exponential
 726 fitting function.

727 Table 7 shows mean values S_{ys} varying from 0.012 nm^{-1} for the Eastern Mediterranean Sea
 728 (EMED) up to 0.019 nm^{-1} for the Baltic Sea (BLTS). The systematic negative biases B_{ys} across
 729 all marine regions are likely explained by the choice of zeroing the original spectra of absorption
 730 coefficients using values averaged in the 670-680 nm spectral interval. High residuals B_{ys} of
 731 0.029 m^{-1} are observed for the Baltic Sea (BLTS). This is explained by a decreased performance
 732 of Eq. 9 when fitting spectra of absorption coefficients exhibiting values approaching or
 733 exceeding 1 m^{-1} at 412 nm. Still, all residuals B_{ys} expressed in percent of A_{ys} vary between 0.3
 734 and 0.5%, except for the East Mediterranean Sea (EMED) showing a value of 0.9%.

735 As expected, also the values of S_b largely vary across the CoASTS and BiOMaP marine
 736 regions: in particular they exhibit values of $2.97 \text{ } \mu\text{m}^{-1}$ for the East Mediterranean Sea (EMED),
 737 $2.06 \text{ } \mu\text{m}^{-1}$ for the Iberian Shelf (IBSH) and $0.74 \text{ } \mu\text{m}^{-1}$ for the North Sea (NORS). This is likely
 738 explained by an increase of the average particles size when going from the oligotrophic East
 739 Mediterranean Sea to the eutrophic and more sediment loaded North Sea.

740 Figure 7 and 8 shows the distribution of *Chla* and *SPM* across the CoASTS and BiOMaP
 741 marine regions. The very low concentrations characterizing the oligotrophic waters of the
 742 Eastern Mediterranean Sea (EMED) exhibiting mean *Chla* values of $0.09 \text{ } \mu\text{g l}^{-1}$ and mean *SPM*
 743 values of 0.27 mg l^{-1} , are remarkable. Conversely, *Chla* exhibits mean values in the range of 4-5
 744 $\mu\text{g l}^{-1}$ for both the North Sea (NORS) and Baltic Sea (BLKS), while for the same marine regions
 745 *SPM* shows mean values of 9.96 and 1.53 mg l^{-1} , respectively. A log-normal distribution of both
 746 *Chla* and *SPM* is generally confirmed for the CoASTS and BiOMaP data.

752 Figure 9 displays the scatter plots of $b_{bp}(488)/b_p(488)$ versus $Chla$, where $b_p(488)$ is
753 determined by the difference between $c_{t-w}(488)$ and $a_{t-w}(488)$, while $b_{bp}(488)$ is determined from
754 $b_b(488)$ by subtracting the scattering coefficient of water $b_w(488)$ from Morel (1974). Results are
755 consistent with those shown by Twardowski et al. (2001) for a variety of experimental data, with
756 $b_{bp}(488)/b_p(488)$ typically varying between 0.003 and 0.025. Exception are some very low
757 values of $b_{bp}(488)/b_p(488)$ for EMED data likely explained by large measurement uncertainties.
758 Coherent with published results is also the generally higher value and higher scatter of
759 $b_{bp}(488)/b_p(488)$ in correspondence of low $Chla$ concentrations.

760
761

762 Table 6. Parameters A_{dt} , S_{dt} and B_{dt} of the exponential fitting function (see Eq. 8) applied to the
763 values of $a_{dt}(\lambda)$. The quantity R_{dt} indicates the spectral average of absolute differences (*i.e.*,
764 residuals) between actual and fitted values.

765

| Region | $A_{dt} [m^{-1}]$ | $S_{dt} [nm^{-1}]$ | $B_{dt} [m^{-1}]$ | $R_{dt} [m^{-1}]$ |
|--------------|-------------------|--------------------|-------------------|-------------------|
| EMED (N=190) | 0.010±0.007 | 0.009±0.002 | 0.002±0.001 | 0.0000 |
| WMED (N=186) | 0.009±0.004 | 0.012±0.001 | 0.003±0.001 | 0.0000 |
| IBSH (N=129) | 0.024±0.022 | 0.011±0.001 | 0.006±0.005 | 0.0001 |
| GRLS (N=54) | 0.024±0.014 | 0.012±0.002 | 0.007±0.004 | 0.0000 |
| LIGS (N=126) | 0.032±0.026 | 0.011±0.002 | 0.007±0.004 | 0.0001 |
| ADRS (N=120) | 0.042±0.057 | 0.012±0.001 | 0.009±0.011 | 0.0000 |
| AAOT (N=614) | 0.048±0.031 | 0.012±0.001 | 0.009±0.005 | 0.0000 |
| BLKS (N=692) | 0.034±0.057 | 0.011±0.002 | 0.005±0.008 | 0.0001 |
| NORS (N=102) | 0.288±0.377 | 0.013±0.001 | 0.067±0.094 | 0.0005 |
| BLTS (N=274) | 0.095±0.125 | 0.011±0.002 | 0.011±0.017 | 0.0003 |

766
767

768 Table 7. Parameters A_{ys} , S_{ys} and B_{ys} of the exponential fitting function (see Eq. 9) applied to the
769 values of $a_{ys}(\lambda)$. The quantity R_{ys} indicates the spectral average of absolute differences (*i.e.*,
770 residuals) between actual and fitted values.

771

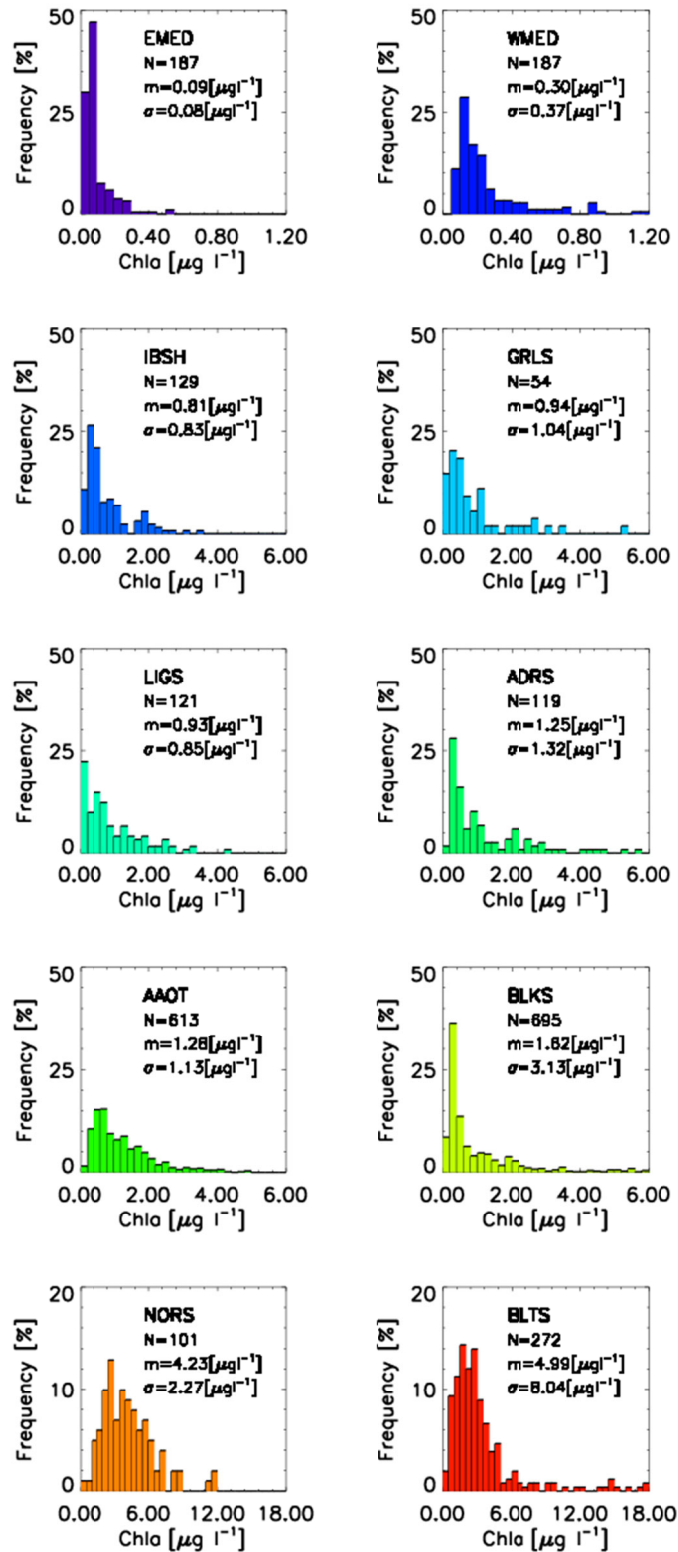
| Region | $A_{ys} [m^{-1}]$ | $S_{ys} [nm^{-1}]$ | $B_{ys} [m^{-1}]$ | $R_{ys} [m^{-1}]$ |
|--------------|-------------------|--------------------|-------------------|-------------------|
| EMED (N=182) | 0.056±0.025 | 0.012±0.004 | -0.005±0.007 | 0.0004 |
| WMED (N=183) | 0.059±0.019 | 0.013±0.003 | -0.002±0.002 | 0.0002 |
| IBSH (N=129) | 0.093±0.036 | 0.014±0.003 | -0.004±0.005 | 0.0004 |
| GRLS (N=54) | 0.107±0.027 | 0.014±0.003 | -0.004±0.003 | 0.0003 |
| LIGS (N=126) | 0.091±0.052 | 0.014±0.004 | -0.004±0.004 | 0.0004 |
| ADRS (N=120) | 0.114±0.058 | 0.016±0.002 | -0.002±0.002 | 0.0003 |
| AAOT (N=592) | 0.132±0.059 | 0.017±0.004 | -0.003±0.005 | 0.0003 |
| BLKS (N=693) | 0.205±0.122 | 0.017±0.002 | -0.004±0.003 | 0.0005 |
| NORS (N=102) | 0.280±0.094 | 0.017±0.002 | -0.004±0.002 | 0.0007 |
| BLTS (N=274) | 0.606±0.330 | 0.019±0.001 | -0.004±0.003 | 0.0029 |

772
773

774 Table 8. Parameters A_b and S_b of the power law fitting function (see Eq. 10) applied to the values
 775 of $b_b(\lambda)$ at $\lambda= 443, 488, 510, 555$ and 620 nm for the CoASTS and BioMaP marine regions. The
 776 quantity R_b indicates the spectral average of absolute differences (*i.e.*, residuals) between actual
 777 and fitted data.

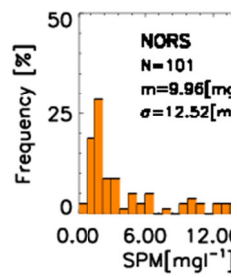
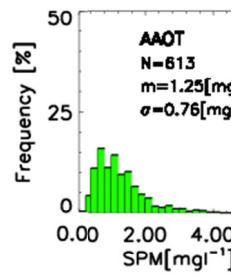
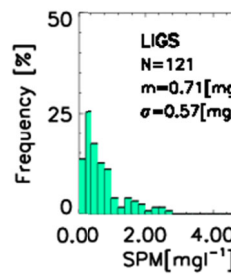
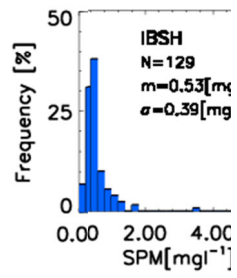
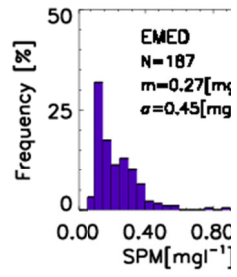
| Region | A_b [m^{-1}] | S_b [μm^{-1}] | R_b [m^{-1}] |
|--------------|--------------------|------------------------|--------------------|
| EMED (N=184) | 0.0034±0.0008 | 2.97±0.56 | 0.0001 |
| WMED (N=186) | 0.0041±0.0009 | 2.54±0.42 | 0.0001 |
| IBSH (N=127) | 0.0051±0.0025 | 2.06±0.55 | 0.0002 |
| GRLS (N=52) | 0.0048±0.0024 | 2.25±0.33 | 0.0001 |
| LIGS (N=126) | 0.0091±0.0072 | 1.83±0.64 | 0.0002 |
| ADRS (N=111) | 0.0103±0.0071 | 1.74±0.57 | 0.0002 |
| AAOT (N=479) | 0.0136±0.0078 | 1.35±0.42 | 0.0004 |
| BLKS (N=534) | 0.0126±0.0077 | 1.99±0.53 | 0.0006 |
| NORS (N=57) | 0.0207±0.0157 | 0.74±0.38 | 0.0005 |
| BLTS (N=256) | 0.0118±0.0082 | 1.15±0.49 | 0.0003 |

778
 779



780
781
782

Figure 7. Frequency distribution of *Chla* across the CoASTS and BioMaP marine regions. N indicates the number of stations, *m* the mean values and σ the standard deviation.



783
 784 Figure 8. Frequency distribution of SPM
 785 indicates the number of stations, m the me